Cell Reports

Twist2-driven chromatin remodeling governs the postnatal maturation of dermal fibroblasts

Graphical abstract

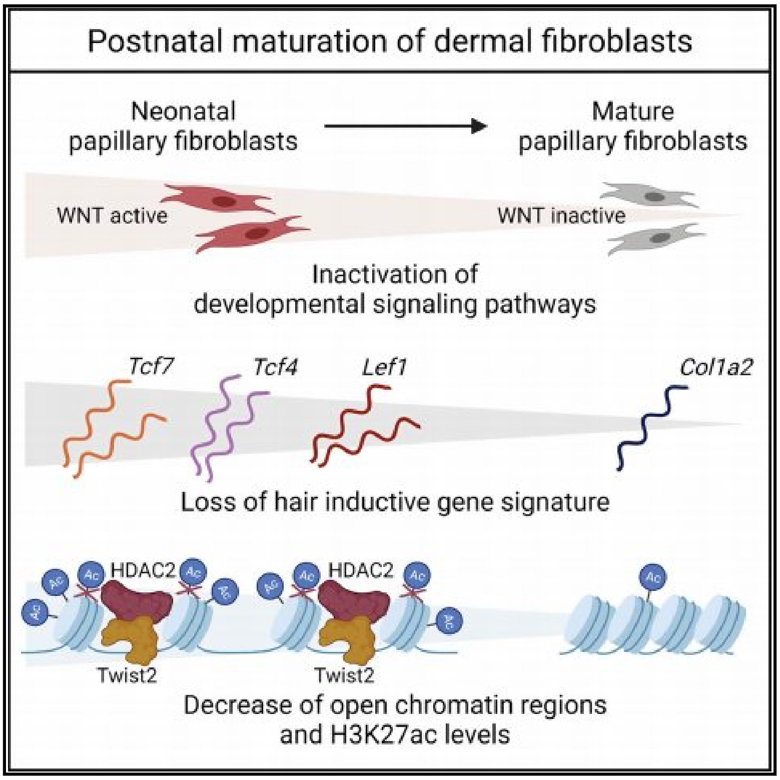

Highlights

- Postnatal papillary fibroblasts lose regenerative ability when H3K27ac levels decrease
- Chromatin accessibility is decreased along with H3K27ac levels in postnatal fibroblasts
- HDAC inhibition delays postnatal chromatin remodeling, which prevents WNT inactivation
- Twist2 deletion in fibroblasts is sufficient to delay the postnatal maturation process

Authors

Jin Yong Kim, Minji Park,
Jungyoon Ohn, ..., Kyu Han Kim,
Seong Jin Jo, Ohsang Kwon

Correspondence

sj.jo@snu.ac.kr (S.J.J.),
oskwon@snu.ac.kr (O.K.)

In brief

Kim et al. show that postnatal papillary fibroblasts lose regenerative ability when H3K27ac levels decrease. Chromatin accessibility is decreased along with H3K27ac modifications. HDAC inhibition delays chromatin remodeling, which prevents postnatal WNT inactivation. Genetic deletion of Twist2 in fibroblasts is sufficient to delay the postnatal maturation process.

Kim et al., 2022, Cell Reports *39*, 110821
May 17, 2022
https://doi.org/10.1016/j.celrep.2022.110821

CellPress

Cell Reports

CellPress
OPEN ACCESS

Article

Twist2-driven chromatin remodeling governs the postnatal maturation of dermal fibroblasts

Jin Yong Kim,[1,2,3,4,8] Minji Park,[1,2,3,5,8] Jungyoon Ohn,[1,2,3] Rho Hyun Seong,[6] Jin Ho Chung,[1,2,3,5] Kyu Han Kim,[1,2,3]
Seong Jin Jo,[1,2,3,*] and Ohsang Kwon[1,2,3,5,7,9,*]
[1]Department of Dermatology, Seoul National University College of Medicine, Seoul 03080, Korea
[2]Laboratory of Cutaneous Aging and Hair Research, Biomedical Research Institute, Seoul National University Hospital, Seoul 03080, Korea
[3]Institute of Human-Environment Interface Biology, Medical Research Center, Seoul National University, Seoul 03080, Korea
[4]Department of Dermatology, Columbia University, New York 10032, NY, USA
[5]Department of Biomedical Sciences, Seoul National University College of Medicine, Seoul 03080, Korea
[6]Department of Biological Sciences, Institute of Molecular Biology and Genetics, Seoul National University, Seoul 08826, Korea
[7]Genomic Medicine Institute, Medical Research Center, Seoul National University College of Medicine, Seoul 03080, Korea
[8]These authors contributed equally
[9]Lead contact
*Correspondence: sj.jo@snu.ac.kr (S.J.J.), oskwon@snu.ac.kr (O.K.)

https://doi.org/10.1016/j.celrep.2022.110821

SUMMARY

Dermal fibroblasts lose stem cell potency after birth, which prevents regenerative healing. However, the underlying intracellular mechanisms are largely unknown. We uncover the postnatal maturation of papillary fibroblasts (PFs) driven by the extensive Twist2-mediated remodeling of chromatin accessibility. A loss of the regenerative ability of postnatal PFs occurs with decreased H3K27ac levels. Single-cell transcriptomics, assay for transposase-accessible chromatin sequencing (ATAC-seq), and chromatin immunoprecipitation sequencing (ChIP-seq) reveal the postnatal maturation trajectory associated with the loss of the regenerative trajectory in PFs, which is characterized by a marked decrease in chromatin accessibility and H3K27ac modifications. Histone deacetylase inhibition delays spontaneous chromatin remodeling, thus maintaining the regenerative ability of postnatal PFs. Genomic analysis identifies Twist2 as a major regulator within chromatin regions with decreased accessibility during the postnatal period. When Twist2 is genetically deleted in dermal fibroblasts, the intracellular cascade of postnatal maturation is significantly delayed. Our findings reveal the comprehensive intracellular mechanisms underlying intrinsic postnatal changes in dermal fibroblasts.

INTRODUCTION

A pool of stem cells (SCs) is preserved to ensure the homeostasis and regeneration of tissues throughout life; however, the stemness of these cells, including their proliferation and differentiation potential, is limited according to their life stage (Ge and Fuchs, 2018; Hanna et al., 2010). Embryonic SCs have the pluripotent ability to generate all cell types in mammals within a few weeks of fertilization. Adult SCs normally retain a certain level of regenerative potential, exclusive to tissue-specific cell types, for decades. *In vivo*, the self-renewal and differentiation potential of cells follows a differentiation hierarchy, from pluripotent SCs and multipotent SCs to fully differentiated cells, from fertilization to senescence throughout the lifetime (Ge and Fuchs, 2018; Hanna et al., 2010).

In the skin, the fetal dermis exhibits a remarkable regenerative ability after tissue injury by reconstituting normal tissue, including the restoration of skin appendages such as functional hair follicles (HFs) (Colwell et al., 2005; Leavitt et al., 2016). However, this regenerative ability is spontaneously lost in the adult dermis by rapid replacement with fibrous scar tissue without HF regeneration after wounding (Driskell et al., 2013; Phan et al., 2020; Rognoni et al., 2016), except at the center of large wounds (Guerrero-Juarez et al., 2019; Ito et al., 2007), which requires the transforming mobilization of latent fibroblasts (Abbasi et al., 2021; Lim et al., 2018) and complex interactions with immune cells (Gay et al., 2013; Guerrero-Juarez et al., 2019) in mice. This spontaneous loss of regenerative ability presumably occurs within the early postnatal period, since the neonatal dermis maintains the ability to regenerate functional HFs (Phan et al., 2020; Rognoni et al., 2016) (Figure S1). Multiple attempts have been made to restore the regenerative ability of dermis by utilizing HF reconstitution assays and wound-induced HF neogenesis models in adult skin (Gay et al., 2013; Ito et al., 2007; Morris et al., 2004). The genetic upregulation of developmental signaling pathways such as WNT and SHH signaling in dermal fibroblasts was shown to enhance their HF regeneration ability in adult skin (Ito et al., 2007; Lim et al., 2018; Phan et al., 2020). However, the intrinsic intracellular mechanisms responsible for the spontaneous loss of regenerative ability in dermal fibroblasts, which may overarch developmental signaling pathways, are largely unknown.

The mouse dermis contains upper and lower fibroblast lineages, which form the upper and lower dermal architectures, respectively, during development and repair processes (Driskell et al., 2013; Plikus et al., 2021). Papillary fibroblasts (PFs), which are located just below the epidermis, are thought to be the primary source of *de novo* HF mesenchyme formation in embryonic skin development and neonatal wound healing (Driskell et al., 2013; Gupta et al., 2019; Mok et al., 2019; Phan et al., 2020). It has been proposed that adult skin forms fibrous scar tissues due to the lack of a defined PF population in the adult dermis (Driskell and Watt, 2015; Salzer et al., 2018). However, it is not fully understood how neonatal PFs lose their initial characteristics, including their inductive properties.

Chromatin is a dynamic structure that regulates the DNA accessibility of transcription factors (TFs) and the transcriptional machinery through multiple levels of structural changes, including histone modifications, during cell transitions or fate commitments (Heintzman et al., 2009; Venkatesh and Workman, 2015). Histone H3K27 acetylation (H3K27ac) is enriched in open accessible chromatin regions and is functionally important for the activity of promoter and enhancer elements (Rada-Iglesias et al., 2011; Zhou et al., 2011). The presence of H3K27ac modification distinguishes active enhancers, suggesting that H3K27ac modification is one of the representative indicators of gene expression during different stages of development (Creyghton et al., 2010). The members of the TWIST TF family are suggested to be the key TFs in early dermal fibroblast progenitors expressed in the embryonic mesoderm starting from embryonic day 9.5 and have been proposed to be regulated in a manner associated with WNT signaling (Budnick et al., 2016; Thulabandu et al., 2018), but their functional role in dermal fibroblasts has not yet been elucidated.

Here, by using HF reconstitution assays, cellular and molecular approaches, single-cell transcriptomics, genomic chromatin accessibility and H3K27ac modification analyses, and a Twist2 genetic mouse model, we reveal an upstream intracellular cascade driving the postnatal maturation of dermal fibroblasts that results in the spontaneous loss of the regenerative ability of PFs after birth.

RESULTS

Postnatal PFs lose their regenerative ability when H3K27ac levels decrease

To determine the time frame in which PFs lose their intrinsic regenerative ability, we performed an HF reconstitution assay (Morris et al., 2004) to minimize the extrinsic bias from latent fibroblasts (Abbasi et al., 2021) or immune interactions (Gay et al., 2013). PFs were sorted by fluorescence-activated cell sorting (FACS) on postnatal days (PDs) 0, 2, and 4 using the CD140a (Pdgfra) and CD26 (Dpp4) surface markers (Driskell et al., 2013) (Figure S2A). CD140a^{+}CD26^{+} PFs were combined with PD0 epidermal keratinocytes and then injected into the back skin of adult immunodeficient BALB/c-nu mice (Figure 1A). After 2 weeks, a number of *de novo* regenerated HFs were observed with PD0 PFs, whereas no HF regeneration was detectable with PD4 PFs (Figures 1B and 1C), showing the spontaneous loss of regenerative ability in postnatal PFs. By utilizing PFs sorted from Pdgfra-H2BGFP mice, we traced the origin of upper fibroblast-lineage cells, which include dermal papilla (DP), dermal sheath, and PFs (Figure 1D), and found that the regenerated HF mesenchyme was derived from grafted H2BGFP^{+} PFs. HF regeneration was not detectable with PD0 epidermal keratinocytes either alone or together with CD140a^{+}CD26^{neg} fibroblasts (Figure S2B and S2C), verifying that PFs are the primary inductive source of HF regeneration. In contrast to the complete loss of HF regeneration with PD4 PFs, a prominent CD140a^{+}CD26^{+} cell population was still detected in the PD4 dermis, suggesting that this loss of HF regeneration was caused by intrinsic cellular changes in inductive source PFs (Figure S2D).

We examined the intrinsic properties of postnatal PFs and found that the expression of Tcf1 and Lef1, the major TFs in the WNT signaling pathway, was lost in PD4 PFs compared with PD0 PFs, which are located below CD49f^{+} basal keratinocytes (Figures 1E and 1F). qRT-PCR showed that the hair inductive gene signature (Higgins et al., 2013; Ohyama et al., 2012), including *Hey1*, *Lef1*, *Ctnnb*, *Wif1*, *Alp*, and *Sox18*, was significantly decreased in PD4 PFs compared with PD0 PFs (Figure 1G). Based on these findings, we postulated that global changes in chromatin accessibility may underlie the simultaneous decrease in the expression of multiple genes in postnatal PFs. To test this hypothesis, we examined markers of histone modification and found that histone H3 acetylation was decreased in PD4 PFs (Figure S2E). Specifically, H3K27ac modification was significantly decreased in PD4 PFs compared with PD0 PFs assessed by the ratio of H3K27ac to H3 expression (Figures 1H and 1I). Decreased H3K27ac levels were consistently observed through the protein analysis of CD140a^{+}CD26^{+} PFs (Figures 1J and 1K). These findings indicated that postnatal PFs lost their regenerative ability when WNT signaling was inactivated, which was accompanied by decreased H3K27ac levels.

Single-cell transcriptomics reveal the postnatal maturation trajectory of PFs

To investigate the intrinsic transcriptomic changes in postnatal PFs, we performed single-cell RNA sequencing (scRNA-seq) on total skin cells isolated on PD0, PD2, and PD4 (Figure 2A). First, mature (spliced) and premature (unspliced) mRNA expression was calculated in each cell, and cells were then clustered based on mature mRNA expression (Bergen et al., 2020) by unsupervised clustering (Hao et al., 2021). A total of 131,956 cells from nine samples (n = 3 biological replicates/time point) met the preprocessing threshold and were divided into 36 clusters of fibroblast-lineage cells and keratinocyte-lineage cells (Figure S3; Table S1). A subset of 59,371 fibroblast-lineage cells was divided into 22 clusters, including PFs, reticular fibroblasts, DP, and dermal sheath (Figures S4A and S4B). Based on the cellular trajectory inferred based on RNA velocity (Bergen et al., 2020) and cluster-specific marker gene expression (Figures S4C and S4D), upper fibroblast-lineage cells were divided into 5 distinct clusters (Fb1, Fb2, Fb3, Dp1, and Dp2) and subjected to downstream analysis (Figure 2B).

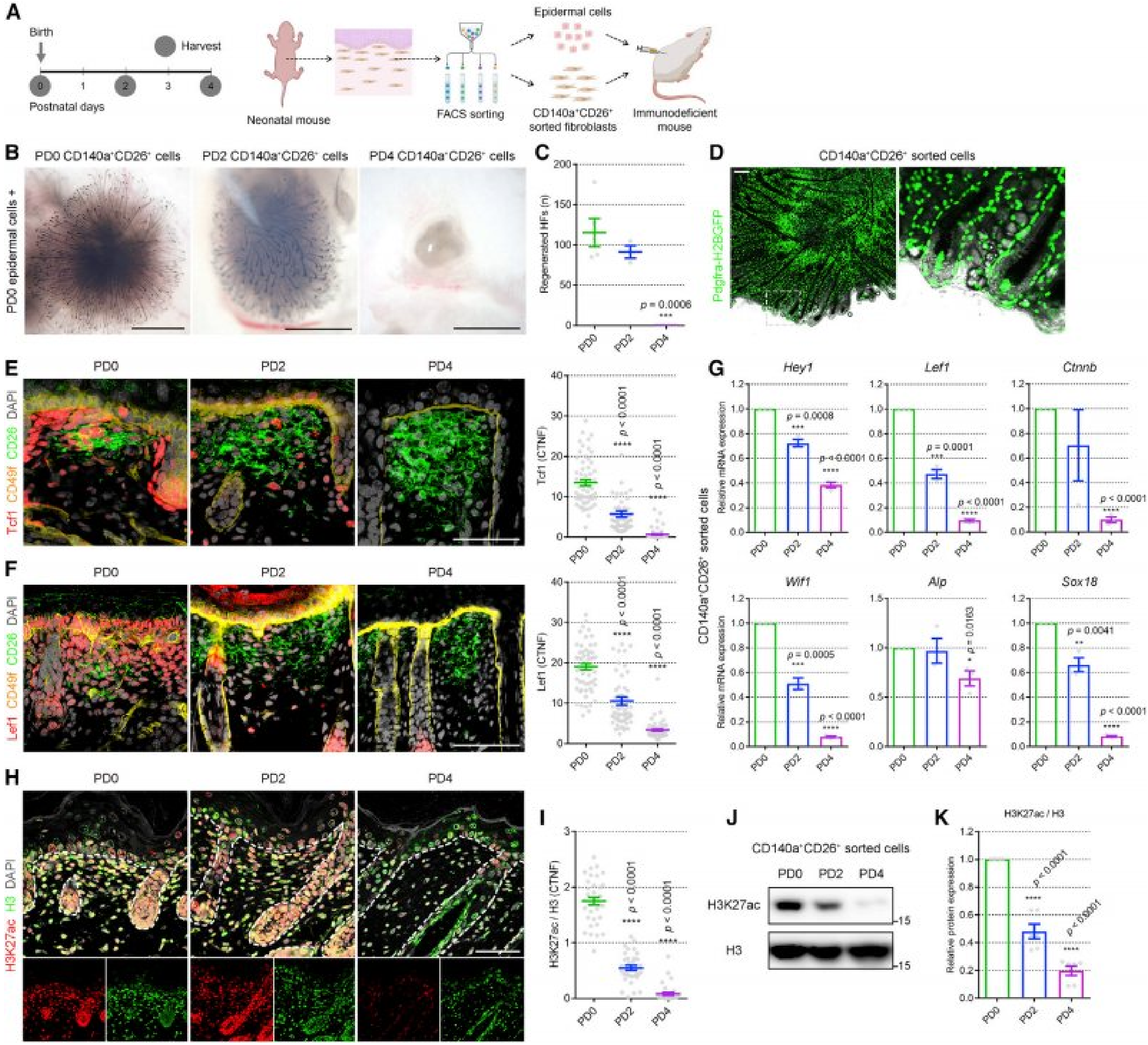

Figure 1. Loss of regenerative ability in PFs accompanied by a decrease in H3K27ac

(A) Experimental scheme of the HF reconstitution assay using PD0, PD2, and PD4 CD140a$^+$CD26$^+$ PFs combined with PD0 epidermal keratinocytes.

(B and C) HF reconstitution assay (B) and quantification of regenerated HFs (C) using CD140a$^+$CD26$^+$ PFs (n = 3–5 replicates/time point), showing that neonatal PFs gradually lost their intrinsic regenerative ability within 4 days of birth.

(D) HF reconstitution assay using CD140a$^+$CD26$^+$ PFs sorted from Pdgfra-H2BGFP mice, showing that the *de novo* HF mesenchyme originated from grafted H2BGFP$^+$ PFs.

(E and F) Immunofluorescence and quantification of the nuclear fluorescence intensity (n = 60 cells/time point) showing significant decreases in Tcf1 and Lef1 expression in PD4 CD26$^+$ PFs compared with PD0 CD26$^+$ PFs, which are located below CD49f$^+$ epidermal keratinocytes.

(G) qRT-PCR showing that the gene expression of *Hey1*, *Lef1*, *Ctnnb*, *Wif1*, *Alp*, and *Sox18* was significantly decreased in PD4 PFs compared with PD0 PFs (n = 3 mice/time point).

(H and I) Immunofluorescence (H) and quantification of the ratio of nuclear H3K27ac and H3 levels (I; n = 34 cells/time point), showing that H3K27ac levels were significantly decreased in PD4 PFs compared with PD0 PFs. Dashed white lines demarcate the dermal-epidermal junction.

(J and K) Western blot (J) and quantification of the ratio of the H3K27ac and H3 protein amounts extracted from CD140a$^+$CD26$^+$ PFs (K; n = 6 mice/time point), showing that H3K27ac levels were significantly decreased in PD4 PFs compared with PD0 PFs. HF, hair follicle; PD, postnatal day; CTNF, corrected total nucleus fluorescence. Scale bars, (B) 1,000 μm, (D) 100 μm, (E, F, H) 50 μm. Data are presented as the mean ± SEM. $^*p < 0.05$, $^{**}p < 0.01$, $^{***}p < 0.001$, $^{****}p < 0.0001$ (two-tailed unpaired t test).

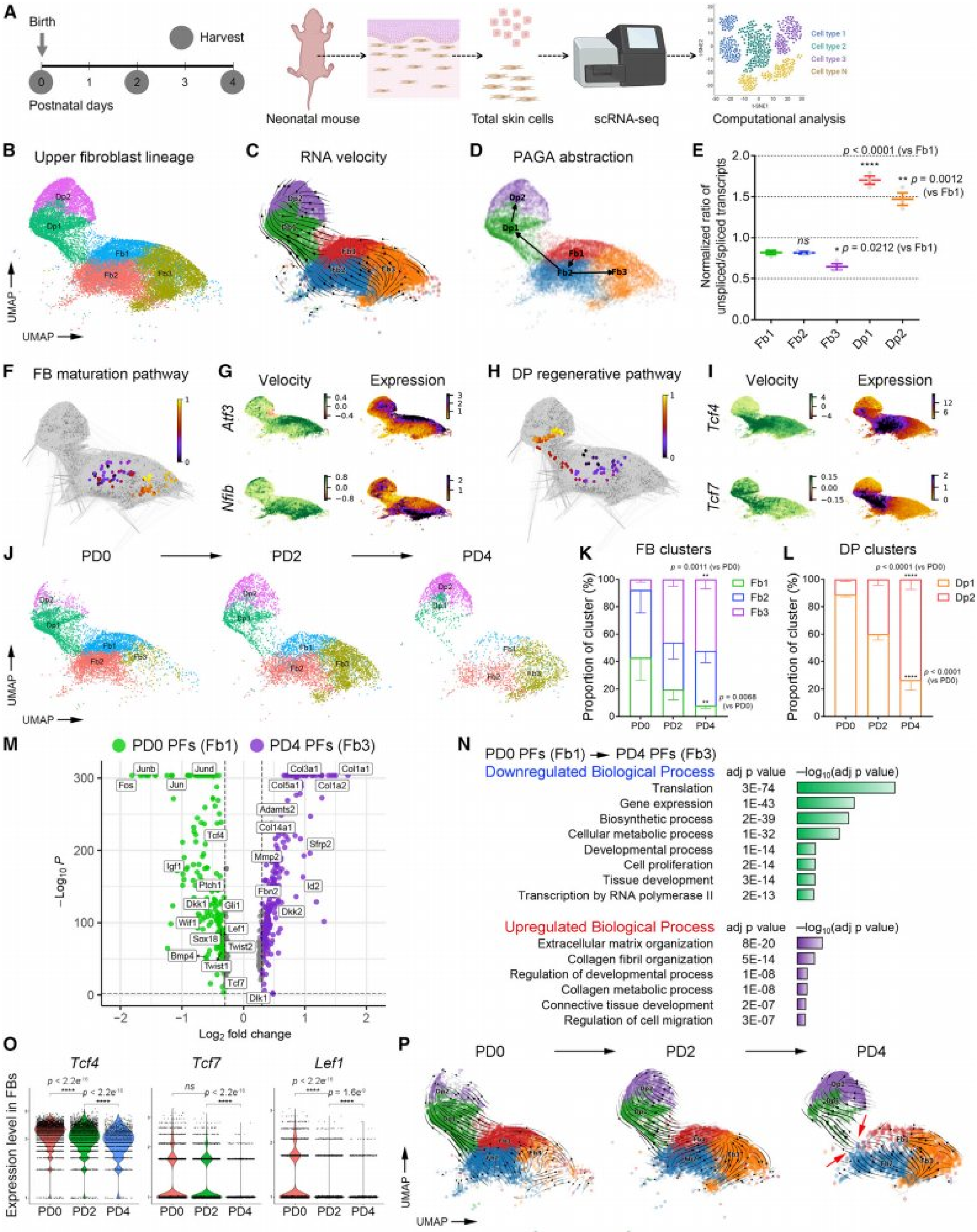

Downregulated Biological Process

	adj p value	−log10(adj p value)
Translation	3E-74	
Gene expression	1E-43	
Biosynthetic process	2E-39	
Cellular metabolic process	1E-32	
Developmental process	1E-14	
Cell proliferation	2E-14	
Tissue development	3E-14	
Transcription by RNA polymerase II	2E-13	

Upregulated Biological Process

	adj p value	−log10(adj p value)
Extracellular matrix organization	8E-20	
Collagen fibril organization	5E-14	
Regulation of developmental process	1E-08	
Collagen metabolic process	1E-08	
Connective tissue development	2E-07	
Regulation of cell migration	3E-07	

(legend on next page)

RNA velocity and partition-based graph abstraction (PAGA) revealed two distinct differentiation trajectories in upper fibroblast-lineage cells: Fb1 → Fb2 → Fb3 (FB maturation pathway) and Fb1 → Fb2 → Dp1 → Dp2 (DP regenerative pathway) (Figures 2C and 2D). The ratio of unspliced/spliced transcripts was significantly lower in Fb3 cells but higher in Dp1 and Dp2 cells than in Fb1 cells (Figure 2E), suggesting that transcriptional activity decreases in the FB maturation pathway but increases in the DP regenerative pathway. Cellular ancestry analysis revealed representative transitional descendants developing toward the FB maturation pathway (Figure 2F) or the DP regenerative pathway (Figure 2H). RNA velocity gene analysis identified Atf3 and Nfib as major TFs in the FB maturation pathway (Figure 2G) and Tcf4 and Tcf7 as major TFs in the DP regenerative pathway (Figure 2I). The inference of TF activities through gene regulatory network analysis (Aibar et al., 2017) showed that Atf3 and Jun are major TFs in the FB maturation pathway and that Tcf7 and Gli1 are major TFs in the DP regenerative pathway (Figures S4E and S4F).

To confirm these differentiation trajectories in the temporal landscape, we examined the proportion of each cluster in PD0, PD2, and PD4 replicates (Figure 2J). FB clusters showed a transition in which an Fb1 decrease was compensated for by an Fb3 increase from PD0 to PD4 (Figure 2K), and DP clusters showed a transition in which a Dp1 decrease was compensated for by a Dp2 increase (Figure 2L), verifying two differentiation trajectories. To define the PD0 PF and PD4 PF signatures, we compared the gene expression profiles of Fb1 cells (representative of PD0 PFs) and Fb3 cells (representative of PD4 PFs). We found that PD0 PF-signature genes, such as *Fos*, *Jun*, *Jund*, *Tcf4*, *Tcf7*, *Lef1*, *Sox18*, *Gli1*, *Ptch1*, *Wif1*, *Bmp4, Twist1*, and *Twist2*, were significantly downregulated, whereas PD4 PF-signature genes, such as *Col1a1*, *Col1a2*, *Col5a1*, *Col14a1*, *Adamts2*, *Mmp2, Dkk2*, *Dlk1*, and *Sfrp2*, were significantly upregulated in PFs during the postnatal period (Figure 2M). As a result, 544 biological processes (Table S2), including translation, gene expression, tissue development, and transcription processes, were downregulated in PD4 PFs compared with PD0 PFs, whereas 137 biological processes (Table S3), including extracellular matrix, collagen fibril organization, and connective tissue development processes, were upregulated (Figure 2N). Reassuringly, the total PD4 PFs (Fb1 + Fb2 + Fb3) showed significantly lower expression of *Tcf4*, *Tcf7*, and *Lef1* than the total PD0 PFs (Fb1 + Fb2 + Fb3) (Figure 2O). Finally, RNA velocity calculated at each time point showed that the FB maturation pathway was the only differentiation trajectory in the PD4 dermis, since the DP regenerative pathway disappeared, in contrast to what was observed in the PD0 dermis (Figure 2P).

Postnatal PFs undergo extensive remodeling of chromatin accessibility

To further determine the mechanisms underlying the spontaneous changes in postnatal PFs, we performed the assay for transposase-accessible chromatin sequencing (ATAC-seq) as well as H3K27ac chromatin immunoprecipitation sequencing (ChIP-seq) using the ChIPmentation (Schmidl et al., 2015) method in CD140a$^+$CD26$^+$ PFs (5×10^4 cells/replicate) sorted on PD0, PD2, and PD4 (Figure 3A). ATAC replicates that met the preprocessing threshold (n = 2 biological replicates/time point) were clustered together within each time point (Figure S5A). The PD0 peaks included 92.2% (40,421 of 43,855) of PD2 peaks, and the PD2 peaks included 98.4% (9,629 of 9,782) of PD4 peaks (Figure 3B), indicating that the PFs mainly lost open chromatin regions from PD0 to PD4, rather than gaining *de novo* open chromatin regions. Genomic annotation revealed that ~78% of PD4 peaks were located in promoter regions and that the PD0 and PD2 peaks located in distal intergenic regions were largely lost in PD4 PFs (Figure S5B), suggesting that the activity of enhancer elements was decreased in PD4 PFs compared with PD0 or PD2 PFs. Overall, chromatin accessibility (Figures S5C and S5D; Table S4) and H3K27ac

Figure 2. Single-cell transcriptome defines the postnatal maturation trajectory of PFs

(A) Experimental scheme of scRNA-seq of total skin cells isolated from PD0, PD2, and PD4 mice (n = 2 mice pooled/replicate, 3 replicates/time point).

(B–D) Uniform Manifold Approximation and Projection (UMAP) of upper fibroblast-lineage clusters (Fb1, Fb2, Fb3, Dp1, and Dp2) identified by unsupervised clustering (B). UMAPs of RNA velocity-inferred cellular trajectory (C) and PAGA abstraction (D) defining two distinct differentiation trajectories in the upper fibroblast lineage: Fb1 → Fb2 → Fb3 (FB maturation pathway) and Fb1 → Fb2 → Dp1 → Dp2 (DP regenerative pathway).

(E) Proportion of spliced and unspliced transcripts in each cluster of cells showing that the ratio of unspliced/spliced transcripts was significantly lower in Fb3 cells but higher in Dp1 and Dp2 cells compared with Fb1 cells.

(F–I) Cellular ancestry analysis revealed representative transitional descendants differentiating toward the FB maturation pathway (F) or DP regenerative pathway (H). Velocity gene analysis identified Atf3 and Nfib as major TFs in the FB maturation pathway (G) and Tcf4 and Tcf7 as major TFs in the DP regenerative pathway (I).

(J–L) UMAP of upper fibroblast-lineage clusters at PD0, PD2, and PD4 (J) and proportions of FB (K) and DP (L) clusters showing a temporal transition in FB clusters, as an Fb1 decrease was compensated for by an Fb3 increase, and a temporal transition in DP clusters, as a Dp1 decrease was compensated for by a Dp2 increase.

(M) Volcano plot showing that PD0 PF (Fb1) signature genes, such as *Fos*, *Jun*, *Jund*, *Tcf4*, *Tcf7*, *Lef1*, *Sox18*, *Gli1*, *Ptch1*, *Wif1*, *Bmp4*, *Twist1*, and *Twist2*, were downregulated, while PD4 PF (Fb3) signature genes, such as *Col1a1*, *Col1a2*, *Col5a1*, *Col14a1*, *Adamts2*, *Mmp2, Dkk2*, *Dlk1*, and *Sfrp2*, were upregulated in PFs during the postnatal period.

(N) Gene ontology analysis showing that translation, gene expression, tissue development, and transcription processes were downregulated in PD4 PFs compared with PD0 PFs, whereas extracellular matrix, collagen fibril organization, and connective tissue development processes were upregulated.

(O) Violin plots showing that total PD4 PFs (Fb1 + Fb2 + Fb3) exhibited significant decreases in *Tcf4*, *Tcf7*, and *Lef1* expression compared with total PD0 PFs.

(P) Cellular trajectory inferred based on RNA velocity calculated at each time point showing that the FB maturation pathway was the only differentiation trajectory in the PD4 dermis, whereas the DP regenerative pathway disappeared, in contrast to the PD0 dermis. PD, postnatal day; PAGA, partition-based graph abstraction; ns, nonsignificant. Data are presented as the mean ± SEM. *$p < 0.05$, **$p < 0.01$, ****$p < 0.0001$ (two-tailed unpaired t test) in (E). **$p < 0.01$, ****$p < 0.0001$ (two-way analysis of variance with Tukey's multiple comparisons test) in (K) and (L). ****$p < 0.0001$ (Wilcoxon two-sample test) in (O).

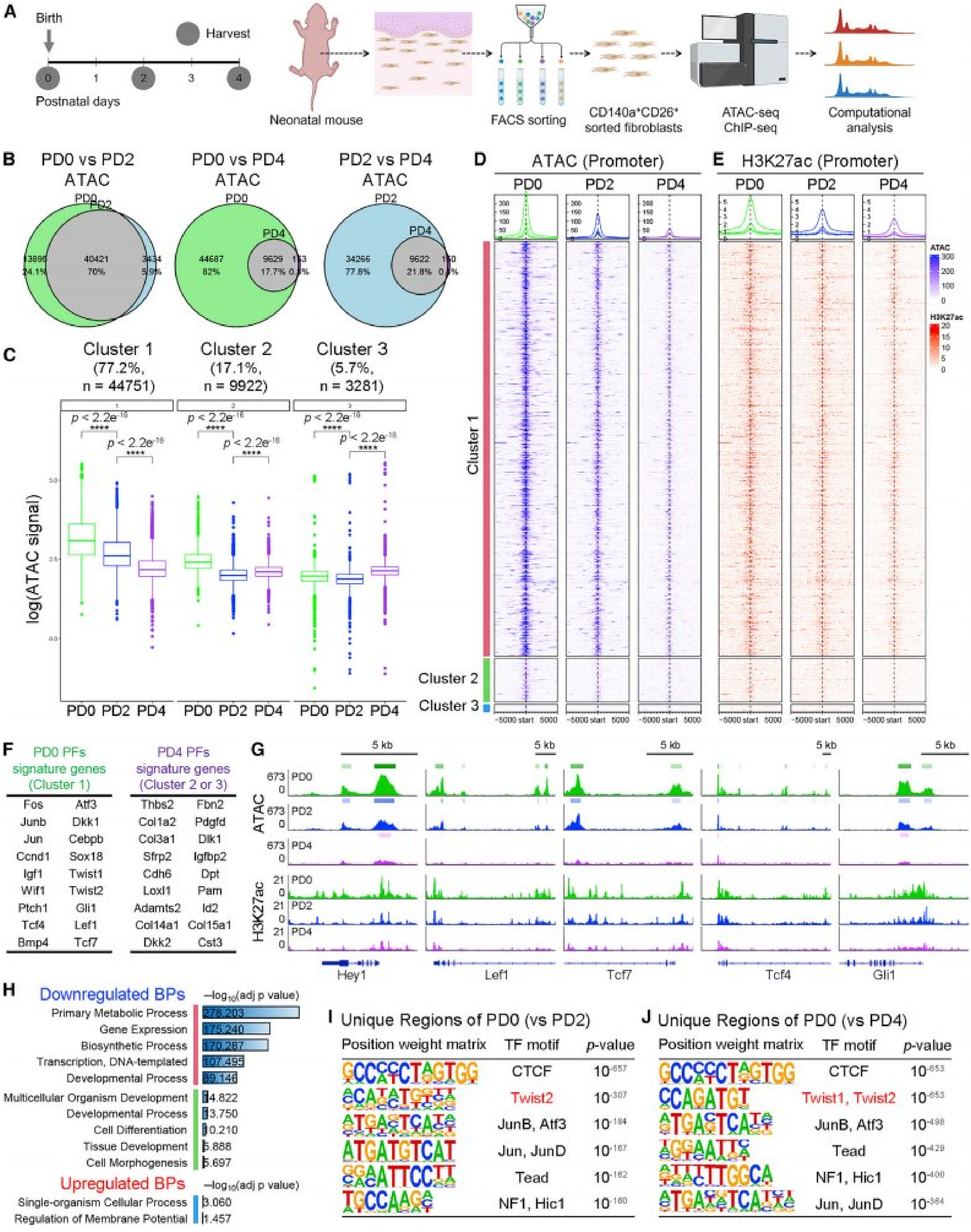

(legend on next page)

modifications (Figure S5E; Table S5) were significantly decreased in PD4 PFs compared with PD0 or PD2 PFs.

We next identified ~58,000 consensus peak regions by merging all PD0, PD2, and PD4 peaks by generating a list of chromatin regions to be compared between time points. Using k-means unsupervised clustering, we divided the consensus peak regions into three cluster domains, in which ATAC signals were decreased in the cluster 1 (77.2%) domain and maintained in the cluster 2 (17.1%) or cluster 3 (5.7%) domains over time (Figures 3C and S5F). Through subset analysis according to the peak annotation, we found that promoter regions were mainly located in the cluster 1 domain and showed significant decreases in chromatin accessibility and H3K27ac modifications over time (Figures 3D and 3E). The distal intergenic regions showed a similar decrease in chromatin accessibility and H3K27ac modifications over time (Figures S5G and S5H). Furthermore, we found that the ATAC signal and H3K27ac signal in each peak region showed positive correlations throughout all time points (Figure S5I).

PD0 PF-signature genes (Figure 2M), such as *Fos*, *Jun*, *Junb*, *Tcf4*, *Tcf7*, *Lef1*, *Sox18*, *Gli1*, *Ptch1*, *Wif1*, *Bmp4*, *Twist1*, and *Twist2*, overlapped with genes annotated based on cluster 1 ATAC peaks (86.3%, 227/263), whereas PD4 PF-signature genes (Figure 2M), such as *Col1a1*, *Col3a1*, *Col14a1*, *Col15a1*, *Adamts2*, *Dkk2*, *Dlk1*, and *Sfrp2*, overlapped with genes annotated based on cluster 2 or cluster 3 ATAC peaks (33.8%, 73/216) (Figure 3F). Specifically, the promoter regions of WNT and SHH TFs, which were grouped with the cluster 1 domain, showed marked loss of chromatin accessibility and H3K27ac modifications (Figure 3G). Gene set ontology analysis revealed that biological processes including primary metabolic processes, gene expression, biosynthetic processes, and transcription (cluster 1) and multicellular organism development, developmental processes, cell differentiation, and tissue development (cluster 2) were significantly downregulated in PD4 PFs relative to PD0 PFs, whereas biological processes including single-organism cellular processes and the regulation of membrane potential were upregulated (Figure 3H), consistent with the ontology results from scRNA-seq analysis (Figure 2N).

The temporal coordination of chromatin accessibility and H3K27ac modifications suggested that these chromatin regions may be distinctly regulated by TFs that are functional in postnatal PFs. To this end, we interrogated the differences in TF motifs and their frequencies of occurrence within PD0-unique regions, which were defined by the subtraction of PD2 peak regions (Figure 3I) or PD4 peak regions (Figure 3J) from PD0 peak regions. We compared the frequencies of PD0-unique regions with those of randomly sampled regions across the whole genome. Notably, TWIST TF family motifs were significantly enriched in PD0-unique regions, which were located next to motifs of CCCTC-binding factor (CTCF), a highly conserved DNA-binding protein required for chromatin loop formation (Ong and Corces, 2014). JunB, Atf3, Jun, Tead, NF1, and Hic1 motifs also showed enrichment within PD0-unique regions; these TFs were previously reported to play roles in the maintenance of cellular identity or deposition of extracellular matrix under homeostatic or wound healing conditions (Abbasi et al., 2021; Atit et al., 1999; Cui et al., 2020; Qin et al., 2018).

In vivo HDAC inhibition delays the loss of regenerative ability in postnatal PFs

Based on the extensive remodeling of chromatin accessibility and H3K27ac modifications underlying the loss of intrinsic regenerative ability, we hypothesized that the inhibition of histone deacetylation may delay the spontaneous intracellular changes in postnatal PFs. Trichostatin A (TSA) is a histone deacetylase HDAC inhibitor that blocks the catalytic cores of these enzymes (Finnin et al., 1999). We subjected neonatal mice to the intraperitoneal injection of TSA (5 μg/g body weight) (Figure 4A). Unexpectedly, the TSA-treated mice showed a notable skin phenotype of thin and less-pigmented skin compared with control littermates (Figure 4B). The histological examination of the TSA-treated PD4 (TSA-PD4) dermis showed dense upper fibroblasts with markedly reduced dermal thickness and atrophic subcutaneous fat compared with control PD4 dermis (Figure 4C), while other skin compartments, such as HFs and the epidermis, continued to develop (Figure 4C). We found that the decrease in nuclear H3K27ac levels was delayed in TSA-PD4 PFs compared with control PD4 PFs, as assessed by the ratio of H3K27ac to H3 expression (Figures 4D and 4E). The delayed decrease in H3K27ac levels was consistently observed in the protein analysis of CD140a$^+$CD26$^+$ PFs (Figures 4F, 4G, and S6A).

Figure 3. Extensive remodeling of chromatin structure in postnatal PFs

(A) Experimental scheme of the ATAC-seq and H3K27ac ChIP-seq of CD140a$^+$CD26$^+$ PFs (5×10^4 cells) sorted from PD0, PD2, and PD4 mice (n = 2 mice pooled/replicate, 2 ATAC replicates/time point).

(B) Venn diagrams showing that PD0 peaks included 92.2% (40,421 of 43,855) of PD2 peaks and PD2 peaks included 98.4% (9,629 of 9,782) of PD4 peaks, indicating that PFs mainly lost open chromatin regions during the postnatal period, rather than gaining *de novo* open chromatin regions.

(C) Boxplots of ATAC signals (log fold change) in each cluster domain showing that ATAC signals were decreased in cluster 1 (77.2%) domain and maintained in cluster 2 (17.1%) or cluster 3 (5.7%) domains over time.

(D and E) Heatmaps of ATAC and H3K27ac signal intensity in promoter regions based on cluster domains.

(F) List of representative PD0 PF signature genes overlapping with genes annotated to cluster 1 ATAC peaks and representative PD4 PF signature genes overlapping with genes annotated to cluster 2 or cluster 3 ATAC peaks.

(G) Representative Integrative Genomics Viewer images showing peaks and ATAC signals and H3K27ac signals at Hey1, Lef1, Tcf7, Tcf4, and Gli1 genomic loci.

(H) Gene ontology analysis showing that primary metabolic processes, gene expression, biosynthetic processes, and transcription (cluster 1) and multicellular organism development, developmental processes, cell differentiation, and tissue development (cluster 2) were significantly downregulated in PD4 PFs relative to PD0 PFs, whereas single-organism cellular processes and the regulation of membrane potential were upregulated.

(I and J) HOMER *de novo* motif analysis of PD0-unique regions, defined by the subtraction of PD2 peak regions or PD4 peak regions from PD0 peak regions, showing that motifs of the TWIST family were significantly enriched in PD0-specific regions. PD, postnatal day; BP, biological process. Data are presented as the means with 25th and 75th percentiles. ****$p < 0.0001$ (two-way analysis of variance) in (C).

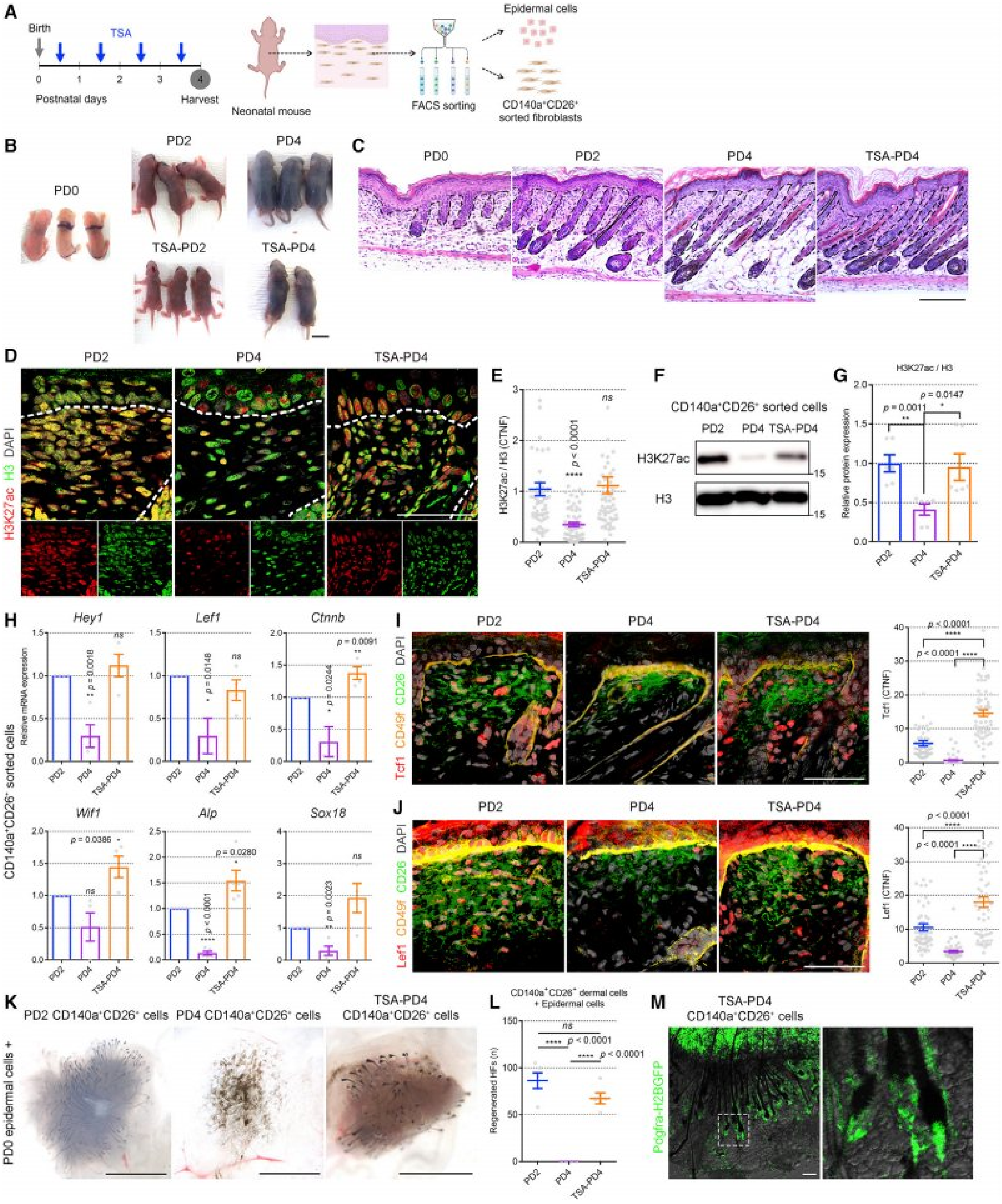

Figure 4. ***In vivo*** **HDAC inhibition delays the loss of the regenerative ability of postnatal PFs**

(A) Experimental scheme of the *in vivo* inhibition of histone deacetylation by the intraperitoneal injection of TSA (5 μg/g body weight) into neonatal mice.

(B) Gross phenotype of TSA-treated mice showing a notable skin phenotype of thin and less-pigmented skin compared with control littermates.

(legend continued on next page)

qRT-PCR showed that loss of the hair-inductive gene signature was delayed in TSA-PD4 PFs relative to control PD4 PFs (Figure 4H). Moreover, the loss of Tcf1 and Lef1 expression was delayed in TSA-PD4 PFs compared with control PD4 PFs (Figures 4I and 4J). We performed an HF reconstitution assay using TSA-PD4 mice and identified a number of regenerated HFs, indicating that the intrinsic regenerative ability was retained on PD4 by TSA treatment (Figures 4K and 4L). We confirmed that the upper fibroblast-lineage cells, including DP, dermal sheath, and PF cells, originated from grafted TSA-PD4 PFs (Figure 4M). These findings demonstrated that the postnatal decreases in H3K27ac levels and chromatin accessibility inactivate the WNT signaling pathway, resulting in the loss of the intrinsic regenerative ability of PFs.

HDAC inhibition delays postnatal chromatin remodeling in PFs

To investigate the transcriptomic changes induced by TSA treatment, we performed scRNA-seq on total skin cells isolated from TSA-PD4 mice (42,260 cells, n = 3 biological replicates) and compared the results with the PD2 and PD4 datasets (Figures 5A and S6B–S6E). We found that the spontaneous changes in FB and DP cluster proportions were significantly delayed in the TSA-PD4 dermis compared with the PD4 dermis (Figures 5B and 5C). Accordingly, TSA-PD4 PFs (Fb1 + Fb2 + Fb3) retained the expression of Tcf4, Tcf7, and Lef1 compared with the levels observed in PD4 PFs and showed similar expression levels compared with PD2 PFs (Figure 5D). Moreover, the RNA velocity calculated for each sample showed that the DP regenerative pathway was retained in the TSA-PD4 dermis, in contrast to the PD4 dermis (Figure 5E).

To evaluate the effect of HDAC inhibition on postnatal chromatin changes, we performed ATAC-seq and H3K27ac ChIP-seq on CD140a$^+$CD26$^+$ PFs sorted from TSA-PD4 mice and compared the results with the PD2 and PD4 datasets. TSA-PD4 ATAC replicates (n = 2 biological replicates) were clustered together in the middle of PD2 and PD4 ATAC replicates (Figure S7A). Notably, TSA-PD4 peaks were included in both the PD0 peaks (99.0%, 18,309 of 18,481) and the PD2 peaks (98.8%, 18,252 of 18,481), whereas the TSA-PD4 peaks included PD4 peaks (94.7%, 9,262 of 9,782) (Figure 5F), indicating that TSA treatment delayed the loss of open chromatin regions in postnatal PFs rather than causing the gain of *de novo* open chromatin regions. Genomic annotation showed that ~58% of TSA-PD4 peaks were located in promoter regions and that ~19% of TSA-PD4 peaks were located in distal intergenic regions, which were spontaneously lost in PD4 PFs during the postnatal period (Figure S7B). Overall, the postnatal changes in chromatin accessibility (Figure S7C; Table S4) and H3K27ac modifications (Figure S7D; Table S5) were significantly delayed in TSA-PD4 PFs compared with PD4 PFs. By analyzing the ATAC signal and H3K27ac signal according to the cluster domains defined based on PD0, PD2, and PD4 samples, we found that the spontaneous changes in chromatin accessibility showed a marked reversal in all three cluster domains by TSA treatment (Figures 5G and S7E). The promoter regions (Figures 5H and 5I) as well as the distal intergenic regions (Figures S7F–S7G) showed a reversal of the spontaneous losses of chromatin accessibility and H3K27ac modifications upon TSA treatment (Figures 5H and 5I). For example, the promoter regions of WNT and SHH TFs retained their accessibility and H3K27ac modifications after TSA treatment (Figure S7H).

We again interrogated the differences in TF motifs and their frequencies within TSA-PD4-unique regions or PD2-unique regions, which were defined by the subtraction of PD4 peak regions from TSA-PD4 peak regions or PD2 peak regions, respectively. Surprisingly, motifs of the TWIST TF family were again found to be significantly enriched in both TSA-PD4-unique regions (Figure 5J) and PD2-unique regions with the highest statistical significance (Figure 5K).

Twist2 expression and chromatin binding decrease in PFs during the postnatal period

To further determine the roles of TWIST TFs in postnatal PFs, we examined the expression of TWIST TFs in upper fibroblast-lineage cells. Twist2 expression was significantly decreased in PD4 PFs compared with PD0 PFs and PD2 PFs, while the loss of Twist2 expression was partially recovered in TSA-PD4 PFs (Figures 6A and 6B). In addition, Twist2 expression was limited to PFs and was not observed in the HF mesenchyme, whereas Twist1 expression was observed in both PFs and the HF mesenchyme (Figures 6A and S4D).

The genomic footprint detected in ATAC-seq refers to a pattern in which an active TF binds chromatin, thus preventing Tn5 transposase-mediated cleavage within the binding site. Similar to nucleosomes, bound TFs result in defined regions of

---

(C) H&E images showing a higher density of upper fibroblasts with markedly reduced dermal thickness and atrophic subcutaneous fat in the TSA-PD4 dermis compared with the control PD4 dermis. Note that other skin compartments, such as HFs or the epidermis, continued to develop (black dashed line).

(D and E) Immunofluorescence evaluation (D) and quantification of the ratio of nuclear H3K27ac and H3 levels (E; n = 62 cells/group), showing that the decrease in H3K27ac levels was significantly delayed in TSA-PD4 PFs compared with control PD4 PFs. Dashed white lines demarcate the dermal-epidermal junction.

(F and G) Western blot (F) and ratio of H3K27ac and H3 protein levels (G) extracted from CD140a$^+$CD26$^+$ PFs (n = 6 mice/group), showing that the decrease in H3K27ac levels was significantly delayed in TSA-PD4 PFs compared with control PD4 PFs.

(H) qRT-PCR results showing that decreases in *Hey1*, *Lef1*, *Ctnnb*, *Wif1*, *Alp*, and *Sox18* gene expression were significantly delayed in TSA-PD4 PFs compared with control PD4 PFs (n = 3–5 mice/group).

(I and J) Immunofluorescence evaluation and quantification of nuclear fluorescence intensity (n = 60 cells/group) showing that loss of Tcf1 and Lef1 expression was significantly delayed in TSA-PD4 PFs compared with control PD4 PFs.

(K and L) HF reconstitution assay (K) and quantification of regenerated HFs (L) using PD2, PD4, and TSA-PD4 CD140a$^+$CD26$^+$ PFs (n = 4–5 replicates/group), showing that the spontaneous loss of regenerative ability in postnatal PFs was significantly delayed by TSA treatment.

(M) HF reconstitution assay of TSA-PD4 CD140a$^+$CD26$^+$ PFs from Pdgfra-H2BGFP mice, showing that the *de novo* HF mesenchyme originated from grafted H2BGFP-expressing PFs. PD, postnatal day; TSA, trichostatin A; CTNF, corrected total nucleus fluorescence; ns, nonsignificant. Scale bars, (B, K) 1,000 μm, (C, M) 100 μm, (D, I, J) 50 μm. Data are presented as the mean ± SEM. $^*p < 0.05$, $^{**}p < 0.01$, $^{****}p < 0.0001$ (two-tailed unpaired t test).

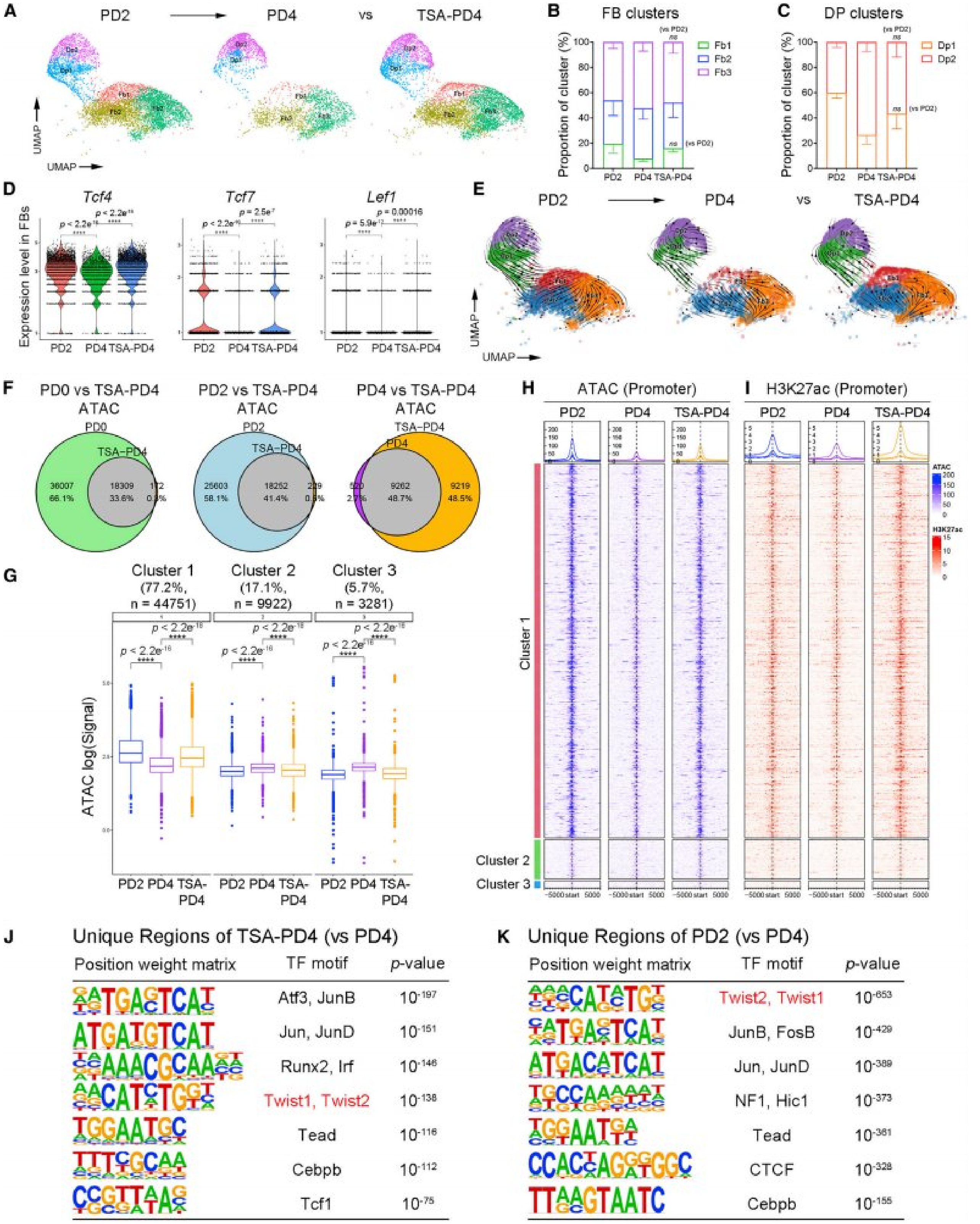

(legend on next page)

decreased ATAC signal strength within larger regions of high ATAC signals (Bentsen et al., 2020; Yan et al., 2020). To obtain further evidence of the chromatin binding activity of Twist2 in open chromatin regions of postnatal PFs, we performed a genomic footprinting analysis of the PD0, PD2, PD4, and TSA-PD4 peak regions. We found that Twist2 footprints were clearly visible in PD0 and PD2 peak regions; however, they were significantly decreased in PD4 peak regions (Figure 6C). Moreover, Twist2 footprints were partially recovered in TSA-PD4 peak regions, consistent with the expression of Twist2 (Figure 6C).

To test the possibility that Twist2 interacts with the HDAC machinery in the unique peak regions lost during the postnatal period, we performed Twist2 coimmunoprecipitation on CD140a$^+$CD26$^+$ PFs. We found that the Twist2 protein complex directly interacts with the HDAC2 enzyme in CD140a$^+$CD26$^+$ PFs (Figures 6D and S8A). Our genomic and coimmunoprecipitation data prompted us to hypothesize that Twist2 may function as a major driver of chromatin remodeling by closing the unique peak regions in postnatal PFs.

Twist2 drives the postnatal maturation of dermal fibroblasts

To test this hypothesis, we generated an inducible Cre-dependent genetic knockout mouse model (Pdgfra-CreER; Twist2$^{flox/flox}$) to delete Twist2 expression in Pdgfra$^+$ dermal fibroblasts. Tamoxifen induction was carried out four times in pregnant mice and neonatal mice near the time of birth (Figures 7A, S8B, and S8C). Pdgfra-Twist2$^{-/-}$ mice showed a notable skin phenotype of thin and less-pigmented skin compared with control littermates (Figure 7B), which we also observed in TSA-treated mice (Figure 4B). Histological examination of the Pdgfra-Twist2$^{-/-}$ PD4 dermis showed dense upper fibroblasts with a markedly reduced dermal thickness and atrophic subcutaneous fat compared with the control PD4 dermis (Figure 7C), while other skin compartments, such as HFs or epidermis, continued to develop (Figures 7C and S8D). Twist2 expression was significantly diminished in Pdgfra-Twist2$^{-/-}$ PFs compared with control PFs (Figures 7D and 7E). Notably, we found that the decrease in nuclear H3K27ac levels was significantly delayed in Pdgfra-Twist2$^{-/-}$ PD4 PFs compared with control PD4 PFs (Figure 7F). qRT-PCR showed that loss of the hair inductive gene signature, including *Hey1*, *Tcf7*, *Lef1*, *Wif1*, and *Alp*, was significantly delayed in Pdgfra-Twist2$^{-/-}$ PD4 PFs compared with control PD4 PFs (Figure 7G). Consistently, the loss of Tcf1 and Lef1 expression was significantly delayed in Pdgfra-Twist2$^{-/-}$ PD4 PFs compared with control PD4 PFs (Figures 7H and 7I). Taken together, our study revealed a role for Twist2 in dermal fibroblasts as the key driver of the postnatal maturation process via the recruitment of a protein complex interacting with HDAC2, resulting in the inactivation of the WNT signaling pathway after birth.

DISCUSSION

SCs are self-renewing progenitors that maintain their ability to give rise to both undifferentiated SCs and more committed descendants (Bradley et al., 2002). Tissue SCs retain some degree of stemness by balancing quiescence, proliferation, and differentiation to maintain and restore tissue integrity after various injuries (Aponte and Caicedo, 2017). The regeneration process requires the recruitment and activation of tissue SCs according to the extent of tissue damage. However, repetitive failure and/or misappropriated regenerative mechanisms often result in unwanted outcomes, such as carcinogenesis (Dvorak, 1986; Schäfer and Werner, 2008), by overwhelming the normal competence of tissue SCs predetermined for tissue repair and regeneration (Coussens and Werb, 2002; Ratajczak et al., 2018; Schäfer and Werner, 2008). Thus, it is thought to be necessary for tissue SCs to maintain their regenerative potential at minimum for survival at specific life stages, especially in the skin, which experiences numerous tissue injuries and subsequent regeneration as the outermost barrier.

During embryonic development, fibroblasts populate the dermal structure via remarkable proliferation (Chen et al., 2012) and form dermal condensates along the regenerative trajectory (Gupta et al., 2019; Mok et al., 2019). In this study, PFs still showed the potential to differentiate toward the HF mesenchyme along the regenerative trajectory for the first few days after birth (Liang et al., 2011; Phan et al., 2020). However, after this time period, which coincided with the time point at which proliferation ceased (Rognoni et al., 2016), most PFs committed to the maturation trajectory while spontaneously losing their initial

Figure 5. HDAC inhibition delays postnatal chromatin remodeling in PFs

(A–C) UMAP of upper fibroblast-lineage clusters in PD2, PD4, and TSA-PD4 samples (A) and proportions of FB (B) and DP (C) clusters showing that the temporal transition in FB clusters and DP clusters was significantly delayed in the TSA-PD4 dermis compared with the control PD4 dermis.

(D) Violin plots showing that TSA-PD4 PFs (Fb1 + Fb2 + Fb3) maintained *Tcf4*, *Tcf7*, and *Lef1* expression levels compared with control PD4 PFs, showing similar levels compared with PD2 PFs.

(E) The cellular trajectory inferred based on RNA velocity calculated for each sample showed that the DP regenerative pathway was retained in the TSA-PD4 dermis in contrast to the control PD4 dermis.

(F) Venn diagrams showing that TSA-PD4 peaks were included in PD0 peaks (99.0%, 18,309 of 18,481) as well as PD2 peaks (98.8%, 18,252 of 18,481), but TSA-PD4 peaks included PD4 peaks (94.7%, 9,262 of 9,782).

(G) Boxplots of ATAC signals (log fold change) in each cluster domain showing that the spontaneous changes in chromatin accessibility were markedly reversed in all three domains by TSA treatment.

(H and I) Heatmaps of ATAC and H3K27ac signal intensity in promoter regions according to cluster domains.

(J and K) HOMER *de novo* motif analysis within TSA-PD4-unique regions or PD2-unique regions, which were defined by the subtraction of PD4 peak regions from TSA-PD4 peak regions or PD2 peak regions, respectively, showing that motifs of the TWIST family were again detected as significantly enriched in TSA-PD4-unique regions as well as PD2-unique regions with the highest statistical significance. PD, postnatal day; TSA, trichostatin A; ns, nonsignificant. Data are the mean ± SEM (two-way analysis of variance with Tukey's multiple comparisons test) in (B) and (C). ****$p < 0.0001$ (Wilcoxon two-sample test) in (D). Data are presented as the means with the 25th and 75th percentiles. ****$p < 0.0001$ (two-way analysis of variance) in (G).

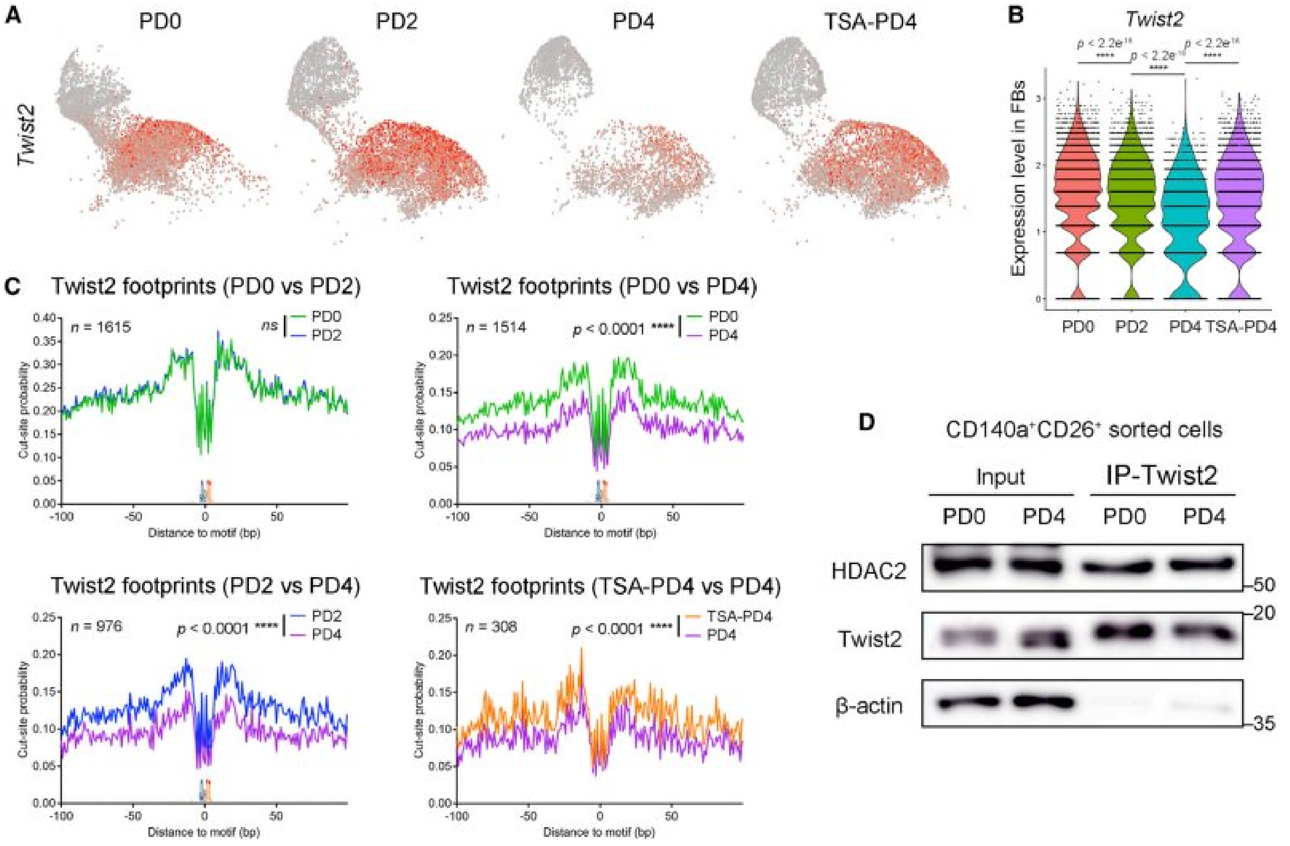

Figure 6. Twist2 expression and chromatin binding are decreased during the postnatal period

(A) Twist2 gene expression in PD0, PD2, PD4, and TSA-PD4 upper fibroblast-lineage clusters (Fb1, Fb2, Fb3, Dp1, and Dp2). Note that Twist2 expression is limited to PFs but not in the HF mesenchyme.

(B) Violin plots showing that Twist2 expression was gradually lost from PD0 PFs (Fb1 + Fb2 + Fb3) to PD4 PFs and that this loss of Twist2 expression was partially recovered in TSA-PD4 PFs.

(C) Genomic footprinting analysis of PD0, PD2, PD4, and TSA-PD4 peak regions showing that Twist2 footprints were clearly visible in PD0 and PD2 peak regions and significantly decreased in PD4 peak regions. Twist2 footprints were partially recovered in TSA-PD4 peak regions, consistent with the Twist2 expression pattern.

(D) Twist2 coimmunoprecipitation and western blot showing that the Twist2 protein complex directly interacts with the HDAC2 enzyme in $CD140a^{+}CD26^{+}$ PFs.

PD, postnatal day; TSA, trichostatin A; ns, nonsignificant. ****$p < 0.0001$ (Wilcoxon two-sample test) in (B). ****$p < 0.0001$ (two-tailed unpaired t test) in (C).

differentiation potential. Indeed, adult fibroblasts demonstrate strong positional and behavioral stability when both are unperturbed or even after neighboring cells are damaged (Marsh et al., 2018). These serial observations could be keys to understanding the postnatal period as a critical turning point for dermal fibroblasts to orchestrate intracellular and behavioral adaptation from embryonic development to the postnatal growth phase. Neonatal PFs lost their regenerative potential to form HF mesenchyme *de novo* during this period and instead became more specialized on the fibrous deposition function for extracellular matrix repair and collagen deposition, resulting in a rapid increase in dermal thickness.

Recently, postnatal maturation was highlighted as a pivotal process for the acquisition of proper cellular and tissue function, as a form of extensive remodeling in chromatin accessibility and corresponding transcriptional changes (Greenberg et al., 2017; Kim et al., 2020; Lattke et al., 2021; Reizel et al., 2018). For the functional maturation of neuronal astrocytes, Rorb, Dbx2, and Lhx2 TFs are required to drive the postnatal maturation program through chromatin reorganization (Lattke et al., 2021). Herein, we demonstrated that Twist2 is required to drive the postnatal maturation process in dermal fibroblasts by reshaping the chromatin landscape, suggesting that dermal fibroblasts are evolutionarily adapted to undergo postdevelopmental molding to acquire their rapid wound healing ability after the completion of major tissue development processes.

TWIST is a member of the basic helix-loop-helix (bHLH) TF family, and bHLH TFs represent the second most populated family of TFs in the human genome (Thurman et al., 2012). The bHLH TFs are classified into seven major classes, including the ubiquitous class I bHLH factors, which dimerize with lineage-restricted class II bHLH partners (de Martin et al., 2021). TWIST forms a subfamily of class II bHLH factors that are capable of binding the conserved sequence 5′-NCANNTGN-3′ (E-box motif) (Chang et al., 2015; Zeid et al., 2018). Many of the target genes of mammalian TWIST have multiple E-box

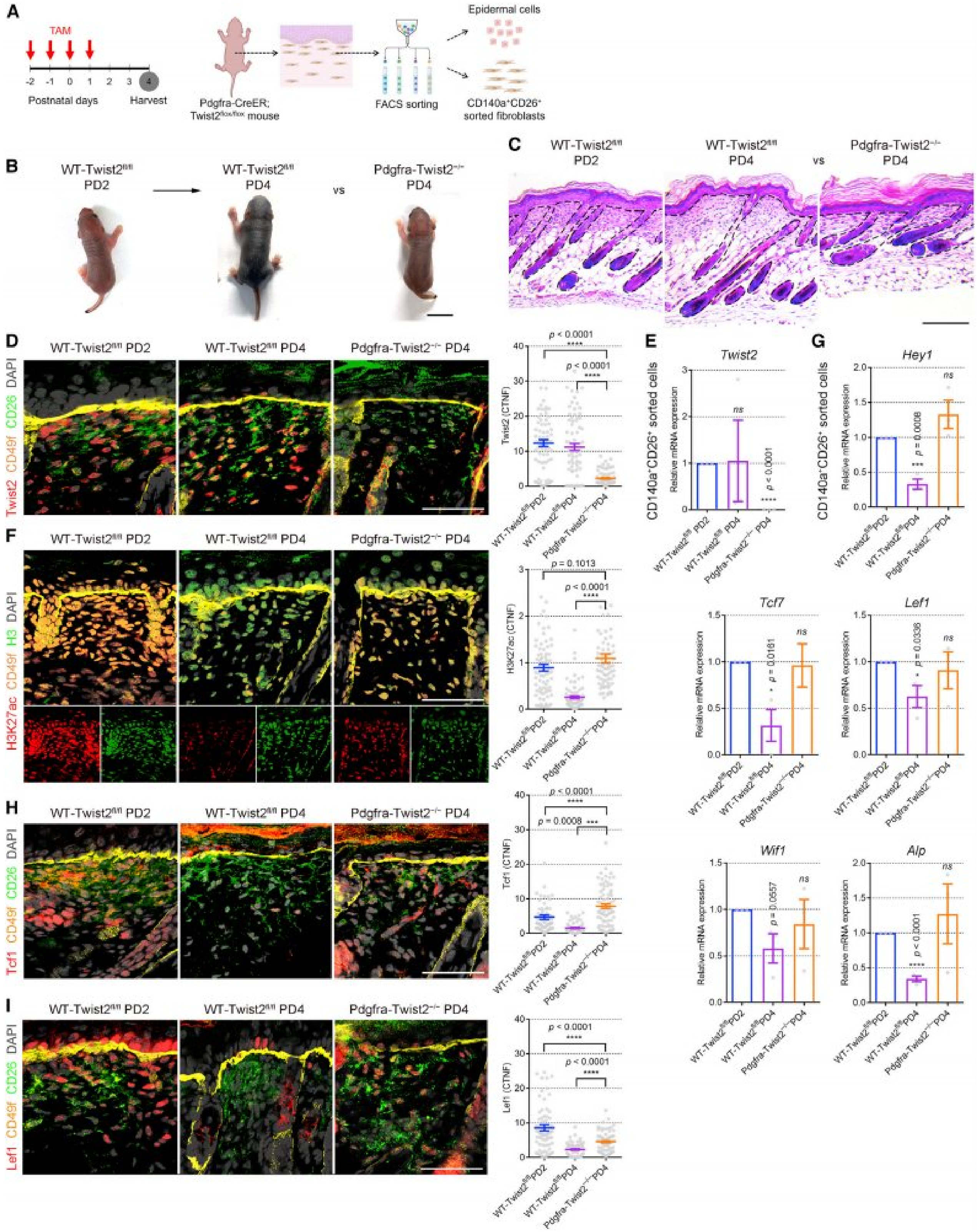

(legend on next page)

sequences in their promoter regions, and the particular bHLH TFs with which TWIST dimerizes influence E-box selection and control transcriptional outcomes (Franco et al., 2011a). Therefore, Twist2 can play bifunctional roles as a repressor of gene transcription through the formation of heterodimers with E12 proteins (class I bHLH factors) (Gong and Li, 2002; Lee et al., 2003) or as an activator of gene transcription by forming functional homodimers (Franco et al., 2011b).

Consistent with our coimmunoprecipitation data, TWIST2 was shown to recruit the nucleosome remodeling and deacetylation (NuRD) protein complex by interacting with E12, MTA2, RbAp46, Mi2, and HDAC2 in human cells (Fu et al., 2011; McDonel et al., 2009). TWIST2 forms heterodimers with E12 and binds E-box motifs of chromatin; the N terminus and the C terminus of TWIST2 interact with MTA2; and the C terminus of MTA2 interacts with HDAC2 (Fu et al., 2011). In the context of postnatal PFs, Twist2 is thought to act as a transcriptional repressor of target genes by recruiting the NuRD complex, which drives postnatal chromatin remodeling by instructing histone deacetylation in the binding site.

The WNT signaling pathway is an evolutionarily conserved intercellular communication system that is important for cell proliferation and differentiation during both development and tissue homeostasis (Steinhart and Angers, 2018). In embryonic development, canonical WNT signaling is required and sufficient for the induction of Twist2 expression in dermal fibroblasts (Budnick et al., 2016; Jacob et al., 2021). In HF morphogenesis, active WNT signaling in dermal fibroblasts through β-catenin and WNT co-TFs, such as Lef1, Tcf1, and Tcf4, is an essential prerequisite for DP commitment (Chen et al., 2012; Gupta et al., 2019; Mok et al., 2019; Phan et al., 2020).

Here, we showed that neonatal PFs still showed regenerative ability, supported by active WNT signaling, at birth, when embryonic HF morphogenesis is complete. During the postnatal period, Twist2-driven chromatin remodeling induced spontaneous intracellular changes following the FB maturation pathway, leading to a loss of regenerative ability mediated by the inactivation of the WNT signaling pathway. Considering that the expression and chromatin binding of Twist2 are decreased during the postnatal maturation process, the major role of Twist2 is suggested to be the lineage-specific inactivation of WNT signaling, which functions in a time-dependent manner after birth. The role of Twist2 is suggested to be partially conserved during wound-induced HF neogenesis in adult skin because Twist2 is differentially expressed in only a subset of Crabp1^{+} upper-wound fibroblasts (Guerrero-Juarez et al., 2019). Furthermore, the transitional loss of Twist2 expression in fibroblasts is thought to be required to sustain high WNT signaling activity after the completion of DP differentiation.

Constitutional Twist2-knockout mice show a distinctive dermal phenotype (Šošić et al., 2003) comparable to that of human Setleis syndrome caused by TWIST2 nonsense mutations (Tukel et al., 2010). Twist2-null mice with a 129/Sv genetic background are indistinguishable from their wild-type littermates at birth but develop notable skin abnormalities, such as dermal atrophy and adipose deficiency, during the postnatal period and die within the first 2 weeks after birth from cachexia (Šošić et al., 2003). However, Twist2-null mice with a 129/C57 mixed genetic background survive and exhibit only mild disease, showing a facial phenotype including thin skin and sparse hair in the bitemporal area, characterized by atrophic dermis and deficient adipose tissue (Tukel et al., 2010). In patients with Setleis syndrome, the diagnostic characteristic is bitemporal scar-like atrophic skin lesions, which are histologically characterized as a type of mesodermal dysplasia with significant reductions in dermal thickness and almost a complete absence of subcutaneous fat. In this study, TSA-treated mice and Pdgfra-Twist2$^{-/-}$ mice showed similar histological findings of reduced dermal thickness and atrophic subcutaneous fat (Figures 4C and 7C). Considering that the reticular dermis and subcutaneous fat also showed significant expansion during the postnatal period, it is likely that Twist2-driven inactivation of the WNT signaling pathway may be required for the postnatal differentiation of both upper and lower fibroblast-lineage cells.

Our study revealed the intracellular mechanism driving postnatal maturation in dermal fibroblasts through the extensive remodeling of chromatin accessibility leading to the inactivation of developmental signaling pathways after birth. By demonstrating that the decrease in H3K27ac levels and subsequent inactivation of WNT signaling were dependent on Twist2 in postnatal PFs, our data suggest that Twist2 acts as a lineage-specific master regulator promoting the postnatal differentiation of

Figure 7. Twist2 governs the postnatal maturation of dermal fibroblasts

(A) Experimental scheme of the Pdgfra-CreER; Twist2$^{flox/flox}$ mouse model in which Twist2 expression was deleted in Pdgfra^{+} fibroblasts. Tamoxifen induction was carried out four times in pregnant mice and neonatal mice close to birth.

(B) Gross phenotype of Pdgfra-Twist2$^{-/-}$ mice showing a notable skin phenotype of thin and less-pigmented skin compared with control littermates, observed in TSA-treated mice.

(C) H&E images showing a higher density of upper fibroblasts with marked reductions in dermal thickness and atrophic subcutaneous fat in the Pdgfra-Twist2$^{-/-}$ PD4 dermis compared with the control PD4 dermis. Note that other skin compartments, such as HFs and the epidermis, continued to develop (black dashed line).

(D and E) Immunofluorescence and quantification of the nuclear fluorescence intensity (D; n = 60 cells/group) and qRT-PCR results (E) showing that Twist2 expression was significantly diminished in the Pdgfra-Twist2$^{-/-}$ dermis (n = 3 mice/group).

(F) Immunofluorescence and quantification of the ratio of nuclear H3K27ac and H3 levels (n = 76 cells/group), showing that the decrease in H3K27ac levels was significantly delayed in Pdgfra-Twist2$^{-/-}$ PD4 PFs compared with control PD4 PFs. Note that nuclear H3K27ac expression was retained only in dermal fibroblasts compared with epidermal keratinocytes.

(G) qRT-PCR results showing that the decrease in *Hey1*, *Tcf7*, *Lef1*, *Wif1*, and *Alp* gene expression was significantly delayed in Pdgfra-Twist2$^{-/-}$ PD4 PFs compared with control PD4 PFs (n = 3 mice/group).

(H and I) Immunofluorescence evaluation and quantification results (n = 60 cells/group) showing that the loss of Tcf1 and Lef1 expression was significantly delayed in Pdgfra-Twist2$^{-/-}$ PD4 PFs compared with control PD4 PFs. PD, postnatal day; CTNF, corrected total nucleus fluorescence; TAM, tamoxifen; ns, nonsignificant. Scale bars, (B) 1 cm, (C) 100 μm, (D, F, H, I) 50 μm. Data are the mean ± SEM. $^{*}p < 0.05$, $^{***}p < 0.001$, $^{****}p < 0.0001$ (two-tailed unpaired t test).

fibroblasts by designating chromatin regions where a loss of accessibility will occur after birth. This study furthers our understanding of the postnatal maturation of cells that previously exhibited regenerative potency, which will potentially give rise to strategies targeting this development process for use in regenerative approaches.

Limitations of the study

Our study showed that the postnatal inactivation of WNT signaling pathways was delayed by TSA treatment by preventing the loss of chromatin accessibility and H3K27ac modifications. However, TSA inhibits the enzymatic activities of the entire HDAC family, including class I and class II HDACs, indicating that the TSA experiment did not specifically target H3K27ac modifications.

We would also like to note that we identified Twist2 footprints in open chromatin regions and their temporal loss during the postnatal period and obtained evidence that Twist2 deletion in dermal fibroblasts was sufficient to delay the postnatal inactivation of developmental signaling pathways by preventing the loss of H3K27ac levels. However, an additional study could be performed to profile the chromatin regions that are directly bound by Twist2 in dermal fibroblasts.

STAR★METHODS

Detailed methods are provided in the online version of this paper and include the following:

- KEY RESOURCES TABLE
- RESOURCE AVAILABILITY
    - ○ Lead contact
    - ○ Material availability
    - ○ Data and code availability
- EXPERIMENTAL MODEL AND SUBJECT DETAILS
    - ○ Experimental model
- METHOD DETAILS
    - ○ Single-cell suspension preparation
    - ○ FACS sorting
    - ○ HF reconstitution assay
    - ○ Histological examination and immunofluorescence staining
    - ○ Real-time qPCR
    - ○ Western blotting
    - ○ Coimmunoprecipitation
    - ○ Single-cell RNA-seq analysis
    - ○ ATAC-seq library preparation
    - ○ ChIP-seq library preparation by ChIPmentation
    - ○ ATAC-seq and ChIP-seq analysis
    - ○ Motif analysis
    - ○ TF footprinting analysis
- QUANTIFICATION AND STATISTICAL ANALYSIS
    - ○ Statistics and reproducibility

SUPPLEMENTAL INFORMATION

Supplemental information can be found online at https://doi.org/10.1016/j.celrep.2022.110821.

ACKNOWLEDGMENTS

This work was supported by a National Research Foundation of Korea (NRF) grant funded by the Korean government (MSIT) (2022R1A2C2004823) and partially supported by the Basic Science Research Program through the National Research Foundation of Korea (NRF) funded by the Ministry of Education (2021R1A6A3A03040183 to J.Y.K.).

AUTHOR CONTRIBUTIONS

J.Y.K. and M.P. designed the studies, performed the experiments, and analyzed and interpreted the data. J.Y.K. performed the computational analysis. J.O. contributed to the experiments. R.H.S. contributed to the Twist2 mouse genetic studies. J.H.C. and K.H.K. discussed the data. S.J.J. and O.K. supervised the project and analyzed and interpreted the data. J.Y.K., M.P., S.J.J., and O.K. wrote the manuscript.

DECLARATION OF INTERESTS

The authors have no conflicts of interest to declare.

Received: December 16, 2021
Revised: March 5, 2022
Accepted: April 22, 2022
Published: May 17, 2022

REFERENCES

Abbasi, S., Sinha, S., Labit, E., Rosin, N.L., Yoon, G., Rahmani, W., Jaffer, A., Sharma, N., Hagner, A., Shah, P., et al. (2021). Distinct regulatory programs control the latent regenerative potential of dermal fibroblasts during wound healing. Cell Stem Cell *28*, 581–583. https://doi.org/10.1016/j.stem.2021.02.004.

Aibar, S., González-Blas, C.B., Moerman, T., Huynh-Thu, V.A., Imrichova, H., Hulselmans, G., Rambow, F., Marine, J.-C., Geurts, P., Aerts, J., et al. (2017). SCENIC: single-cell regulatory network inference and clustering. Nat. Methods *14*, 1083–1086. https://doi.org/10.1038/nmeth.4463.

Aponte, P.M., and Caicedo, A. (2017). Stemness in cancer: stem cells, cancer stem cells, and their microenvironment. Stem Cells Int. *2017*, 1–17. https://doi.org/10.1155/2017/5619472.

Atit, R.P., Crowe, M.J., Greenhalgh, D.G., Wenstrup, R.J., and Ratner, N. (1999). The Nf1 tumor suppressor regulates mouse skin wound healing, fibroblast proliferation, and collagen deposited by fibroblasts. J. Invest. Dermatol. *112*, 835–842. https://doi.org/10.1046/j.1523-1747.1999.00609.x.

Bentsen, M., Goymann, P., Schultheis, H., Klee, K., Petrova, A., Wiegandt, R., Fust, A., Preussner, J., Kuenne, C., Braun, T., et al. (2020). ATAC-seq footprinting unravels kinetics of transcription factor binding during zygotic genome activation. Nat. Commun. *11*, 4267. https://doi.org/10.1038/s41467-020-18035-1.

Bergen, V., Lange, M., Peidli, S., Wolf, F.A., and Theis, F.J. (2020). Generalizing RNA velocity to transient cell states through dynamical modeling. Nat. Biotechnol. *38*, 1408–1414. https://doi.org/10.1038/s41587-020-0591-3.

Bradley, J.A., Bolton, E.M., and Pedersen, R.A. (2002). Stem cell medicine encounters the immune system. Nat. Rev. Immunol. *2*, 859–871. https://doi.org/10.1038/nri934.

Budnick, I., Hamburg-Shields, E., Chen, D., Torre, E., Jarrell, A., Akhtar-Zaidi, B., Cordovan, O., Spitale, R.C., Scacheri, P., and Atit, R.P. (2016). Defining the identity of mouse embryonic dermal fibroblasts. Genesis *54*, 415–430. https://doi.org/10.1002/dvg.22952.

Buenrostro, J.D., Wu, B., Chang, H.Y., and Greenleaf, W.J. (2015). ATAC-seq: a method for assaying chromatin accessibility genome-wide. Curr. Protoc. Mol. Biol. *109*, 21–29. https://doi.org/10.1002/0471142727.mb2129s109.

Carroll, T., and Barrows, D. (2021). Profileplyr: Visualization and Annotation of Read Signal over Genomic Ranges with Profileplyr (Bioconductor version: Release (3.14)) (Bioconductor). https://bioconductor.org/packages/profileplyr/.

Chang, A.T., Liu, Y., Ayyanathan, K., Benner, C., Jiang, Y., Prokop, J.W., Paz, H., Wang, D., Li, H.-R., Fu, X.-D., et al. (2015). An evolutionarily conserved DNA architecture determines target specificity of the TWIST family bHLH transcription factors. Genes Dev. *29*, 603–616. https://doi.org/10.1101/gad.242842.114.

Chen, D., Jarrell, A., Guo, C., Lang, R., and Atit, R. (2012). Dermal β-catenin activity in response to epidermal Wnt ligands is required for fibroblast proliferation and hair follicle initiation. Development *139*, 1522–1533. https://doi.org/10.1242/dev.076463.

Colwell, A.S., Longaker, M.T., and Lorenz, H.P. (2005). Mammalian fetal organ regeneration. Adv. Biochem. Eng. Biotechnol. *93*, 83–100. https://doi.org/10.1007/b99972.

Coussens, L.M., and Werb, Z. (2002). Inflammation and cancer. Nature *420*, 860–867. https://doi.org/10.1038/nature01322.

Creyghton, M.P., Cheng, A.W., Welstead, G.G., Kooistra, T., Carey, B.W., Steine, E.J., Hanna, J., Lodato, M.A., Frampton, G.M., Sharp, P.A., et al. (2010). Histone H3K27ac separates active from poised enhancers and predicts developmental state. Proc. Natl. Acad. Sci. U S A. *107*, 21931–21936. https://doi.org/10.1073/pnas.1016071107.

Cui, L., Chen, S.-Y., Lerbs, T., Lee, J.-W., Domizi, P., Gordon, S., Kim, Y.-H., Nolan, G., Betancur, P., and Wernig, G. (2020). Activation of JUN in fibroblasts promotes pro-fibrotic programme and modulates protective immunity. Nat. Commun. *11*, 2795. https://doi.org/10.1038/s41467-020-16466-4.

Dharmalingam, G., Barrows, D., and Carroll, T. (2021). soGGi: visualise ChIP-seq, MNase-Seq and Motif Occurrence as Aggregate Plots Summarised over Grouped Genomic Intervals (Bioconductor version: Release (3.14)) (Bioconductor). https://bioconductor.org/packages/soGGi/.

Driskell, R.R., and Watt, F.M. (2015). Understanding fibroblast heterogeneity in the skin. Trends Cell Biol. *25*, 92–99. https://doi.org/10.1016/j.tcb.2014.10.001.

Driskell, R.R., Lichtenberger, B.M., Hoste, E., Kretzschmar, K., Simons, B.D., Charalambous, M., Ferron, S.R., Herault, Y., Pavlovic, G., Ferguson-Smith, A.C., and Watt, F.M. (2013). Distinct fibroblast lineages determine dermal architecture in skin development and repair. Nature *504*, 277–281. https://doi.org/10.1038/nature12783.

Dvorak, H.F. (1986). Tumors: wounds that do not heal. Similarities between tumor stroma generation and wound healing. N. Engl. J. Med. *315*, 1650–1659. https://doi.org/10.1056/NEJM198612253152606.

Finnin, M.S., Donigian, J.R., Cohen, A., Richon, V.M., Rifkind, R.A., Marks, P.A., Breslow, R., and Pavletich, N.P. (1999). Structures of a histone deacetylase homologue bound to the TSA and SAHA inhibitors. Nature *401*, 188–193. https://doi.org/10.1038/43710.

Franco, H.L., Casasnovas, J., Rodríguez-Medina, J.R., and Cadilla, C.L. (2011a). Redundant or separate entities?–roles of Twist1 and Twist2 as molecular switches during gene transcription. Nucleic Acids Res. *39*, 1177–1186. https://doi.org/10.1093/nar/gkq890.

Franco, H.L., Casasnovas, J.J., Leon, R.G., Friesel, R., Ge, Y., Desnick, R.J., and Cadilla, C.L. (2011b). Nonsense mutations of the bHLH transcription factor TWIST2 found in Setleis Syndrome patients cause dysregulation of periostin. Int. J. Biochem. Cell Biol *43*, 1523–1531. https://doi.org/10.1016/j.biocel.2011.07.003.

Fu, J., Qin, L., He, T., Qin, J., Hong, J., Wong, J., Liao, L., and Xu, J. (2011). The TWIST/Mi2/NuRD protein complex and its essential role in cancer metastasis. Cell Res. *21*, 275–289. https://doi.org/10.1038/cr.2010.118.

Gay, D., Kwon, O., Zhang, Z., Spata, M., Plikus, M.V., Holler, P.D., Ito, M., Yang, Z., Treffeisen, E., Kim, C.D., et al. (2013). Fgf9 from dermal γδ T cells induces hair follicle neogenesis after wounding. Nat. Med. *19*, 916–923. https://doi.org/10.1038/nm.3181.

Ge, Y., and Fuchs, E. (2018). Stretching the limits: from homeostasis to stem cell plasticity in wound healing and cancer. Nat. Rev. Genet. *19*, 311–325. https://doi.org/10.1038/nrg.2018.9.

Gong, X.Q., and Li, L. (2002). Dermo-1, a multifunctional basic helix-loop-helix protein, represses MyoD transactivation via the HLH domain, MEF2 interaction, and chromatin deacetylation. J. Biol. Chem. *277*, 12310–12317. https://doi.org/10.1074/jbc.m110228200.

Greenberg, M.V.C., Glaser, J., Borsos, M., Marjou, F.E., Walter, M., Teissandier, A., and Bourc'his, D. (2017). Transient transcription in the early embryo sets an epigenetic state that programs postnatal growth. Nat. Genet. *49*, 110–118. https://doi.org/10.1038/ng.3718.

Guerrero-Juarez, C.F., Dedhia, P.H., Jin, S., Ruiz-Vega, R., Ma, D., Liu, Y., Yamaga, K., Shestova, O., Gay, D.L., Yang, Z., et al. (2019). Single-cell analysis reveals fibroblast heterogeneity and myeloid-derived adipocyte progenitors in murine skin wounds. Nat. Commun. *10*, 650. https://doi.org/10.1038/s41467-018-08247-x.

Gupta, K., Levinsohn, J., Linderman, G., Chen, D., Sun, T.Y., Dong, D., Taketo, M.M., Bosenberg, M., Kluger, Y., Choate, K., and Myung, P. (2019). Single-cell analysis reveals a hair follicle dermal niche molecular differentiation trajectory that begins prior to morphogenesis. Dev. Cell *48*, 17–31.e6. https://doi.org/10.1016/j.devcel.2018.11.032.

Gusmao, E.G., Allhoff, M., Zenke, M., and Costa, I.G. (2016). Analysis of computational footprinting methods for DNase sequencing experiments. Nat. Methods *13*, 303–309. https://doi.org/10.1038/nmeth.3772.

Hanna, J.H., Saha, K., and Jaenisch, R. (2010). Pluripotency and cellular reprogramming: facts, hypotheses, unresolved issues. Cell *143*, 508–525. https://doi.org/10.1016/j.cell.2010.10.008.

Hao, Y., Hao, S., Andersen-Nissen, E., Mauck, W.M., Zheng, S., Butler, A., Lee, M.J., Wilk, A.J., Darby, C., Zager, M., et al. (2021). Integrated analysis of multimodal single-cell data. Cell *184*, 3573–3587.e29. https://doi.org/10.1016/j.cell.2021.04.048.

Heintzman, N.D., Hon, G.C., Hawkins, R.D., Kheradpour, P., Stark, A., Harp, L.F., Ye, Z., Lee, L.K., Stuart, R.K., Ching, C.W., et al. (2009). Histone modifications at human enhancers reflect global cell-type-specific gene expression. Nature *459*, 108–112. https://doi.org/10.1038/nature07829.

Heinz, S., Benner, C., Spann, N., Bertolino, E., Lin, Y.C., Laslo, P., Cheng, J.X., Murre, C., Singh, H., and Glass, C.K. (2010). Simple combinations of lineage-determining transcription factors prime cis-regulatory elements required for macrophage and B cell identities. Mol. Cell *38*, 576–589. https://doi.org/10.1016/j.molcel.2010.05.004.

Higgins, C.A., Chen, J.C., Cerise, J.E., Jahoda, C.A.B., and Christiano, A.M. (2013). Microenvironmental reprogramming by three-dimensional culture enables dermal papilla cells to induce de novo human hair-follicle growth. Proc. Natl. Acad. Sci. U S A. *110*, 19679–19688. https://doi.org/10.1073/pnas.1309970110.

Hwang, S., Lee, C., Park, K., Oh, S., Jeon, S., Kang, B., Kim, Y., Oh, J., Jeon, S.H., Satake, M., et al. (2020). Twist2 promotes CD8+ T-cell differentiation by repressing ThPOK expression. Cell Death Differ. *27*, 3053–3064. https://doi.org/10.1038/s41418-020-0560-x.

Ito, M., Yang, Z., Andl, T., Cui, C., Kim, N., Millar, S.E., and Cotsarelis, G. (2007). Wnt-dependent de novo hair follicle regeneration in adult mouse skin after wounding. Nature *447*, 316–320. https://doi.org/10.1038/nature05766.

Jacob, T., Chakravarty, A., Panchal, A., Patil, M., Ghodadra, G., Sudhakaran, J., and Nuesslein-Volhard, C. (2021). Zebrafish twist2/dermo1 regulates scale shape and scale organization during skin development and regeneration. Cells Dev. *166*, 203684. https://doi.org/10.1016/j.cdev.2021.203684.

Kim, J.Y., Kang, B.M., Lee, J.S., Park, H.-J., Wi, H.J., Yoon, J.-S., Ahn, C., Shin, S., Kim, K.H., Jung, K.C., and Kwon, O. (2019). UVB-induced depletion of donor-derived dendritic cells prevents allograft rejection of immune-privileged hair follicles in humanized mice. Am. J. Transpl. *19*, 1344–1355. https://doi.org/10.1111/ajt.15207.

Kim, D.W., Washington, P.W., Wang, Z.Q., Lin, S.H., Sun, C., Ismail, B.T., Wang, H., Jiang, L., and Blackshaw, S. (2020). The cellular and molecular landscape of hypothalamic patterning and differentiation from embryonic to late postnatal development. Nat. Commun. *11*, 4360. https://doi.org/10.1038/s41467-020-18231-z.

Langmead, B., and Salzberg, S.L. (2012). Fast gapped-read alignment with Bowtie 2. Nat. Methods *9*, 357–359. https://doi.org/10.1038/nmeth.1923.

Lattke, M., Goldstone, R., Ellis, J.K., Boeing, S., Jurado-Arjona, J., Marichal, N., MacRae, J.I., Berninger, B., and Guillemot, F. (2021). Extensive transcriptional and chromatin changes underlie astrocyte maturation in vivo and in culture. Nat. Commun. *12*, 4335. https://doi.org/10.1038/s41467-021-24624-5.

Leavitt, T., Hu, M.S., Marshall, C.D., Barnes, L.A., Lorenz, H.P., and Longaker, M.T. (2016). Scarless wound healing: finding the right cells and signals. Cell Tissue Res. *365*, 483–493. https://doi.org/10.1007/s00441-016-2424-8.

Lee, Y.S., Lee, H.H., Park, J., Yoo, E.J., Glackin, C.A., Choi, Y.I., Jeon, S.H., Seong, R.H., Park, S.D., and Kim, J.B. (2003). Twist2, a novel ADD1/SREBP1c interacting protein, represses the transcriptional activity of ADD1/SREBP1c. Nucleic Acids Res. *31*, 7165–7174. https://doi.org/10.1093/nar/gkg934.

Li, Z., Schulz, M.H., Look, T., Begemann, M., Zenke, M., and Costa, I.G. (2019). Identification of transcription factor binding sites using ATAC-seq. Genome Biol. *20*, 45. https://doi.org/10.1186/s13059-019-1642-2.

Liang, Y., Silva, K.A., Kennedy, V., and Sundberg, J.P. (2011). Comparisons of mouse models for hair follicle reconstitution. Exp. Dermatol. *20*, 1011–1015. https://doi.org/10.1111/j.1600-0625.2011.01366.x.

Lim, C.H., Sun, Q., Ratti, K., Lee, S.-H., Zheng, Y., Takeo, M., Lee, W., Rabbani, P., Plikus, M.V., Cain, J.E., et al. (2018). Hedgehog stimulates hair follicle neogenesis by creating inductive dermis during murine skin wound healing. Nat. Commun. *9*, 4903. https://doi.org/10.1038/s41467-018-07142-9.

Love, M.I., Huber, W., and Anders, S. (2014). Moderated estimation of fold change and dispersion for RNA-seq data with DESeq2. Genome Biol. *15*, 550. https://doi.org/10.1186/s13059-014-0550-8.

La Manno, G., Soldatov, R., Zeisel, A., Braun, E., Hochgerner, H., Petukhov, V., Lidschreiber, K., Kastriti, M.E., Lönnerberg, P., Furlan, A., et al. (2018). RNA velocity of single cells. Nature *560*, 494–498. https://doi.org/10.1038/s41586-018-0414-6.

Marsh, E., Gonzalez, D.G., Lathrop, E.A., Boucher, J., and Greco, V. (2018). Positional stability and membrane occupancy define skin fibroblast homeostasis *in vivo*. Cell *175*, 1620–1633.e13. https://doi.org/10.1016/j.cell.2018.10.013.

de Martin, X., Sodaei, R., and Santpere, G. (2021). Mechanisms of binding specificity among bHLH transcription factors. Int. J. Mol. Sci. *22*, 9150. https://doi.org/10.3390/ijms22179150.

McDonel, P., Costello, I., and Hendrich, B. (2009). Keeping things quiet: roles of NuRD and Sin3 co-repressor complexes during mammalian development. Int. J. Biochem. Cell Biol *41*, 108–116. https://doi.org/10.1016/j.biocel.2008.07.022.

Mok, K.-W., Saxena, N., Heitman, N., Grisanti, L., Srivastava, D., Muraro, M.J., Jacob, T., Sennett, R., Wang, Z., Su, Y., et al. (2019). Dermal condensate niche fate specification occurs prior to formation and is placode progenitor dependent. Dev. Cell *48*, 32–48.e5. https://doi.org/10.1016/j.devcel.2018.11.034.

Morris, R.J., Liu, Y., Marles, L., Yang, Z., Trempus, C., Li, S., Lin, J.S., Sawicki, J.A., and Cotsarelis, G. (2004). Capturing and profiling adult hair follicle stem cells. Nat. Biotechnol. *22*, 411–417. https://doi.org/10.1038/nbt950.

Ohyama, M., Kobayashi, T., Sasaki, T., Shimizu, A., and Amagai, M. (2012). Restoration of the intrinsic properties of human dermal papilla in vitro. J. Cell Sci. *125*, 4114–4125. https://doi.org/10.1242/jcs.105700.

Ong, C.-T., and Corces, V.G. (2014). CTCF: an architectural protein bridging genome topology and function. Nat. Rev. Genet. *15*, 234–246. https://doi.org/10.1038/nrg3663.

Orlando, D.A., Chen, M.W., Brown, V.E., Solanki, S., Choi, Y.J., Olson, E.R., Fritz, C.C., Bradner, J.E., and Guenther, M.G. (2014). Quantitative ChIP-Seq normalization reveals global modulation of the epigenome. Cell Rep. *9*, 1163–1170. https://doi.org/10.1016/j.celrep.2014.10.018.

Ou, J., Liu, H., Yu, J., Kelliher, M.A., Castilla, L.H., Lawson, N.D., and Zhu, L.J. (2018). ATACseqQC: a Bioconductor package for post-alignment quality assessment of ATAC-seq data. BMC Genomics *19*, 169. https://doi.org/10.1186/s12864-018-4559-3.

Phan, Q.M., Fine, G.M., Salz, L., Herrera, G.G., Wildman, B., Driskell, I.M., and Driskell, R.R. (2020). Lef1 expression in fibroblasts maintains developmental potential in adult skin to regenerate wounds. Elife *9*, e60066. https://doi.org/10.7554/elife.60066.

Plikus, M.V., Wang, X., Sinha, S., Forte, E., Thompson, S.M., Herzog, E.L., Driskell, R.R., Rosenthal, N., Biernaskie, J., and Horsley, V. (2021). Fibroblasts: origins, definitions, and functions in health and disease. Cell *184*, 3852–3872. https://doi.org/10.1016/j.cell.2021.06.024.

Qin, Z., Xia, W., Fisher, G.J., Voorhees, J.J., and Quan, T. (2018). YAP/TAZ regulates TGF-β/Smad3 signaling by induction of Smad7 via AP-1 in human skin dermal fibroblasts. Cell Commun. Signal *16*, 18. https://doi.org/10.1186/s12964-018-0232-3.

Rada-Iglesias, A., Bajpai, R., Swigut, T., Brugmann, S.A., Flynn, R.A., and Wysocka, J. (2011). A unique chromatin signature uncovers early developmental enhancers in humans. Nature *470*, 279–283. https://doi.org/10.1038/nature09692.

Ramírez, F., Ryan, D.P., Grüning, B., Bhardwaj, V., Kilpert, F., Richter, A.S., Heyne, S., Dündar, F., and Manke, T. (2016). deepTools2: a next generation web server for deep-sequencing data analysis. Nucleic Acids Res. *44*, W160–W165. https://doi.org/10.1093/nar/gkw257.

Ratajczak, M.Z., Bujko, K., Mack, A., Kucia, M., and Ratajczak, J. (2018). Cancer from the perspective of stem cells and misappropriated tissue regeneration mechanisms. Leukemia *32*, 2519–2526. https://doi.org/10.1038/s41375-018-0294-7.

Reizel, Y., Sabag, O., Skversky, Y., Spiro, A., Steinberg, B., Bernstein, D., Wang, A., Kieckhaefer, J., Li, C., Pikarsky, E., et al. (2018). Postnatal DNA demethylation and its role in tissue maturation. Nat. Commun. *9*, 2040. https://doi.org/10.1038/s41467-018-04456-6.

Rognoni, E., Gomez, C., Pisco, A.O., Rawlins, E.L., Simons, B.D., Watt, F.M., and Driskell, R.R. (2016). Inhibition of β-catenin signalling in dermal fibroblasts enhances hair follicle regeneration during wound healing. Development *143*, 2522–2535. https://doi.org/10.1242/dev.131797.

Salzer, M.C., Lafzi, A., Berenguer-Llergo, A., Youssif, C., Castellanos, A., Solanas, G., Peixoto, F.O., Stephan-Otto Attolini, C., Prats, N., Aguilera, M., et al. (2018). Identity noise and adipogenic traits characterize dermal fibroblast aging. Cell *175*, 1575–1590.e22. https://doi.org/10.1016/j.cell.2018.10.012.

Schäfer, M., and Werner, S. (2008). Cancer as an overhealing wound: an old hypothesis revisited. Nat. Rev. Mol. Cell Biol. *9*, 628–638. https://doi.org/10.1038/nrm2455.

Schmidl, C., Rendeiro, A.F., Sheffield, N.C., and Bock, C. (2015). ChIPmentation: fast, robust, low-input ChIP-seq for histones and transcription factors. Nat. Methods *12*, 963–965. https://doi.org/10.1038/nmeth.3542.

Šošić, D., Richardson, J.A., Yu, K., Ornitz, D.M., and Olson, E.N. (2003). Twist regulates cytokine gene expression through a negative Feedback loop that represses NF-κB activity. Cell *112*, 169–180. https://doi.org/10.1016/s0092-8674(03)00002-3.

Steinhart, Z., and Angers, S. (2018). Wnt signaling in development and tissue homeostasis. Development *145*, dev146589. https://doi.org/10.1242/dev.146589.

Thulabandu, V., Chen, D., and Atit, R.P. (2018). Dermal fibroblast in cutaneous development and healing. Wiley Interdiscip. Rev. Dev. Biol. *7*, e307. https://doi.org/10.1002/wdev.307.

Thurman, R.E., Rynes, E., Humbert, R., Vierstra, J., Maurano, M.T., Haugen, E., Sheffield, N.C., Stergachis, A.B., Wang, H., Vernot, B., et al. (2012). The accessible chromatin landscape of the human genome. Nature *489*, 75–82. https://doi.org/10.1038/nature11232.

Tukel, T., Šošić, D., Al-Gazali, L.I., Erazo, M., Casasnovas, J., Franco, H.L., Richardson, J.A., Olson, E.N., Cadilla, C.L., and Desnick, R.J. (2010). Homozygous nonsense mutations in TWIST2 cause Setleis syndrome. Am. J. Hum. Genet. *87*, 289–296. https://doi.org/10.1016/j.ajhg.2010.07.009.

Venkatesh, S., and Workman, J.L. (2015). Histone exchange, chromatin structure and the regulation of transcription. Nat. Rev. Mol. Cell Biol *16*, 178–189. https://doi.org/10.1038/nrm3941.

Wolf, F.A., Hamey, F.K., Plass, M., Solana, J., Dahlin, J.S., Göttgens, B., Rajewsky, N., Simon, L., and Theis, F.J. (2019). PAGA: graph abstraction reconciles clustering with trajectory inference through a topology preserving map of single cells. Genome Biol. *20*, 59. https://doi.org/10.1186/s13059-019-1663-x.

Yan, F., Powell, D.R., Curtis, D.J., and Wong, N.C. (2020). From reads to insight: a hitchhiker's guide to ATAC-seq data analysis. Genome Biol. *21*, 22. https://doi.org/10.1186/s13059-020-1929-3.

Yu, G., Wang, L.-G., and He, Q.-Y. (2015). ChIPseeker: an R/Bioconductor package for ChIP peak annotation, comparison and visualization. Bioinformatics *31*, 2382–2383. https://doi.org/10.1093/bioinformatics/btv145.

Zeid, R., Lawlor, M.A., Poon, E., Reyes, J.M., Fulciniti, M., Lopez, M.A., Scott, T.G., Nabet, B., Erb, M.A., Winter, G.E., et al. (2018). Enhancer invasion shapes MYCN-dependent transcriptional amplification in neuroblastoma. Nat. Genet. *50*, 515–523. https://doi.org/10.1038/s41588-018-0044-9.

Zhang, Y., Liu, T., Meyer, C.A., Eeckhoute, J., Johnson, D.S., Bernstein, B.E., Nusbaum, C., Myers, R.M., Brown, M., Li, W., and Liu, X.S. (2008). Model-based analysis of ChIP-seq (MACS). Genome Biol. *9*, R137. https://doi.org/10.1186/gb-2008-9-9-r137.

Zhou, V.W., Goren, A., and Bernstein, B.E. (2011). Charting histone modifications and the functional organization of mammalian genomes. Nat. Rev. Genet. *12*, 7–18. https://doi.org/10.1038/nrg2905.

STAR★METHODS

KEY RESOURCES TABLE

REAGENT or RESOURCE	SOURCE	IDENTIFIER
Antibodies		
Rabbit polyclonal anti-histone 3 antibody, unconjugated	Abcam	Cat #ab1791, RRID: AB_302613
Goat polyclonal anti-histone 3 antibody, unconjugated	Abcam	Cat #ab12079, RRID: AB_298834
Rabbit polyclonal anti-acetyl-histone H3, unconjugated	Millipore	Cat #06-599, RRID: AB_2115283
Rabbit monoclonal anti-histone H3(acetyl K27)	Abcam	Cat #ab177178, RRID: AB_2828007
Rabbit monoclonal anti-TCF1, unconjugated	Cell Signaling	Cat #2203, RRID: AB_2199302
Rabbit monoclonal anti-LEF1, unconjugated	Cell Signaling	Cat #2230, RRID: AB_823558
Goat polyclonal anti-CD26, unconjugated	R&D systems	Cat #AF954, RRID: AB_355739
Rat monoclonal anti-CD49f, Alexa488 conjugated	BioLegend	Cat #313608, RRID: AB_493635
Mouse monoclonal anti-Twist2, unconjugated	Abnova	Cat #H00117581-M01, RRID: AB_426125
Rat monoclonal anti-CD140a antibody, PE-conjugated	BD	Cat #562776, RRID: AB_2737787
Rat monoclonal anti-CD140a antibody, APC-conjugated	Thermo Fisher	Cat #17-1401-81, RRID:AB_529482
Rat monoclonal anti-CD26 antibody, PE-conjugated	Miltenyi Biotec	Cat #130-119-652, RRID: AB_2733793
Rat monoclonal anti-CD26 antibody, PerCP Cyanine5.5-conjugated	Thermo Fisher	Cat #45-0261-82, RRID: AB_1548738
Rat monoclonal anti-CD45 antibody, biotin-conjugated	Thermo Fisher	Cat #13-0451-81, RRID: AB_466445
Rat monoclonal anti-CD34 antibody, biotin-conjugated	Thermo Fisher	Cat #13-0341-82, RRID: AB_466425
Rat monoclonal anti-CD326 antibody, biotin-conjugated	BioLegend	Cat #118203, RRID: AB_1134174
anti- APC-Cy7, streptavidin-conjugated	BioLegend	Cat #45-0261-82, RRID: N/A
Rabbit polyclonal anti-HDAC2, unconjugated	Santa Cruz	Cat #sc-7899, RRID: AB_2118563
Mouse monoclonal anti-HDAC2, unconjugated	Cell Signaling	Cat #5113, RRID: AB_10624871
anti-beta actin, unconjugated	Thermo Fisher	Cat #MA5-15739, RRID: AB_10979409
Rabbit polyclonal anti-Twist2, unconjugated	Abcam	Cat #ab66031, RRID: AB_2211862
Rabbit polyclonal H3K27ac antibody	Diagenode	Cat #C15410196, RRID: AB_2637079
normal rabbit IgG antibody	Millipore	Cat #NI01-100UG, RRID: AB_10681285
Chemicals, peptides, and recombinant proteins		
Bovine serum albumin	EMD Millipore	Cat #126593
Normal donkey serum	Jackson ImmunoResearch	Cat #017-000-121
NuRD complex ab kit	Cell Signaling	Cat #8349
Triton X-100 solution	Sigma–Aldrich	Cat #X100
Tamoxifen	Sigma–Aldrich	Cat #T5648
Corn oil	Sigma–Aldrich	Cat #C8267
4′,6-Diamidino-2-Phenylindole, Dilactate (DAPI)	BioLegend	Cat #422801
ProLong Gold Antifade Mountant	Thermo Fisher	Cat #P36930
Dimethyl sulfoxide (DMSO)	Sigma–Aldrich	Cat #D2650
Fetal Bovine Serum (FBS)	Thermo Fisher	Cat #16000-044
Phosphate buffered saline (PBS)	Thermo Fisher	Cat #70-013-032
Hank's balanced salt solution (HBSS)	Thermo Fisher	Cat #14-175-095
Deposited data		
Single-cell RNA-seq data	This paper	GEO: GSE181390
ATAC-seq data	This paper	GEO: GSE181394

(*Continued on next page*)

Continued

REAGENT or RESOURCE	SOURCE	IDENTIFIER
H3K27ac ChIP-seq data	This paper	GEO: GSE181394
Experimental models: Organisms/strains		
Mouse: C57BL/6NCrlCrljOri	OrientBio	RRID: N/A
Mouse: CAnN.Cg-Foxn1^{nu}/CrlCrljOri	OrientBio	RRID: N/A
Mouse: B6N.Cg-Tg(Pdgfra-cre/ERT)467Dbe/J	The Jackson Laboratory	Cat# JAX_018280, RRID: IMSR_JAX:018280
Mouse: B6.129S4-Pdgfra$^{tm11(EGFP)Sor}$/J	The Jackson Laboratory	Cat# JAX_007669, RRID: IMSR_JAX:007669
Mouse: Twist2$^{flox/flox}$ mice	Hwang et al., 2020	RRID: N/A
Software and algorithms		
GraphPad Prism 7	GraphPad	https://www.graphpad.com/scientific-software/prism/
ImageJ/FIJI	National Institutes of Health	https://imagej.nih.gov/ij/, https://imagej.net/Fiji
BioRender	BioRender	http://www.biorender.com
CellRanger v4.0.0	10× Genomics	https://support.10xgenomics.com/single-cell-gene-expression/software/
velocyto v0.17	La Manno et al., 2018	http://velocyto.org/
Seurat v4.0	Hao et al., 2021	https://satijalab.org/seurat/
scVelo v0.2.3	Bergen et al., 2020	https://scvelo.readthedocs.io/
SCENIC v1.2.4	Aibar et al., 2017	https://scenic.aertslab.org/
Bowtie2 v1.1.1	Langmead and Salzberg, 2012	http://bowtie-bio.sourceforge.net/bowtie2/
Picard v2.7.1	Broad Institute	https://github.com/broadinstitute/picard
ATACseqQC v1.18.0	Ou et al., 2018	https://bioconductor.org/packages/ATACseqQC/
MACS2 v2.1.2	Heintzman et al., 2009	https://github.com/macs3-project/MACS/
DESeq2 v1.32.0	Love et al., 2014	https://bioconductor.org/packages/DESeq2/
soGGi v1.24.1	Dharmalingam et al., 2021	https://bioconductor.org/packages/soGGi/
ChIPseeker v1.28.3	Yu et al., 2015	https://bioconductor.org/packages/ChIPseeker/
Deeptools v3.4.2	Ramírez et al., 2016	https://deeptools.readthedocs.io/en/develop/index.html
Profileplyr v1.7.0	Carroll and Barrows, 2021	https://bioconductor.org/packages/profileplyr/

RESOURCE AVAILABILITY

Lead contact

Further information and requests for resources and reagents should be directed to and will be fulfilled by the lead contact, Ohsang Kwon (oskwon@snu.ac.kr).

Material availability

This study did not generate new unique reagents.

Data and code availability

- The scRNA-seq, ATAC-seq, and ChIP-seq data have been deposited at NCBI Gene Expression Omnibus (GEO) archive and are publicly available as of the date of publication. Accession numbers are listed in the key resources table.
- This paper does not report original code. Any additional information required to reanalyze the data reported in this paper is available from the lead contact upon request.

EXPERIMENTAL MODEL AND SUBJECT DETAILS

Experimental model

Mice

Adult female C57BL/6J (6–8 weeks) and male BALB/c-nude (5–6 weeks) mice were obtained from OrientBio, Korea. Pdgfra-CreER and Pdgrfa-H2BGFP transgenic mice were obtained from The Jackson Laboratory (JAX stock nos. 018280 and 007669). Twist2-floxed mice were obtained from the Institute of Molecular Biology and Genetics, Seoul National University, Korea (Hwang et al., 2020). We performed experiments using all postnatal mice (PD0, PD2 and PD4) with the appropriate genotype for the study design regardless of sex. For *in vivo* HDAC inhibition, TSA (Sigma) was administered by intraperitoneal injection (5 μg/g body weight). For Cre induction, tamoxifen in corn oil solution (20 mg/mL) was administered by intraperitoneal injection (75 μg/g body weight). All control mice received the same dose of tamoxifen (WT; Twist2flox/flox and Pdgfra-CreER; Twist2flox/flox) as the experimental mice. The mice were maintained under specific pathogen-free conditions. All animal procedures were approved by the Institutional Animal Care and Use Committee of Seoul National University Hospital, Korea. Mice were housed in individually ventilated cages at a maximum density of five mice per cage and maintained under a 12 h–12 h light–dark cycle at a temperature of 18–23°C and 40–60% humidity. None of the mice had been subjected to any other procedures prior to the study. Twist2-floxed mice were genotyped using the following primers: 5′-CGCCAGGTACATAGACTTCC-3′ and 5′-ATTCCGAACGGATACCCTTG-3′.

METHOD DETAILS

Single-cell suspension preparation

After the mice were sacrificed, their entire back skin was harvested, and the subcutaneous fat was removed. The skin tissue was treated with 1 mg/mL Dispase II (Roche) in PBS for 30 min at 37°C to separate the epidermis from the dermis. The dermis was incubated on a plate containing 0.125 mg/mL Liberase TL (Roche) in PBS for 30 min at 37°C. The epidermis was transferred to a conical tube containing 0.25% trypsin (Gibco) in PBS and incubated for 15 min at 37°C. Both the dermal and epidermal suspensions were filtered through 100-μm and 40-μm cell strainers to collect dissociated cells.

FACS sorting

Dermal single-cell suspensions were incubated with FcR blocking solution in 1% BSA buffer for 30 min at 4°C. For the isolation of PFs, the cells were labeled with conjugated anti-EpCAM, anti-CD34, anti-CD45, anti-CD140a, and anti-CD26 (see the key resources table) antibodies in FACS buffer for 30 min on ice. FACS sorting was performed on a FACSAria II instrument (BD) equipped with FACSDiva software (BD), and the data were analyzed with FlowJo software (BD).

HF reconstitution assay

Dissociated epidermal and dermal cells were counted and combined at a 1:2 ratio, and a total of 3×10^6 cells were subcutaneously transplanted into the back skin of 6-week-old BALB/c-nu mice. After 2 weeks, the back skin was harvested, and the regenerated HFs were photographed under a dissecting microscope (Nikon) and quantified using ImageJ/FIJI (NIH).

Histological examination and immunofluorescence staining

For histological examination, back skin was harvested, fixed in 4% paraformaldehyde, embedded in paraffin, sectioned at an 8-μm thickness and stained with hematoxylin and eosin (H&E). For immunofluorescence analysis, back skin was harvested and fixed in 4% paraformaldehyde for 1 h on ice and frozen in OCT. Sections were cut at a thickness of 10 μm with a cryotome (Leica). After washing with PBS, the sections were permeabilized with 0.5% Triton X-100/PBS for 15 min at 25°C and then blocked with 0.5% normal donkey serum (Sigma) for 1 h at 25°C. The samples were incubated with primary antibodies targeting H3 (1:100), H3ac (1:100), H3K27ac (1:100), CD26 (1:200), CD49f (1:100), Tcf1 (1:100), Lef1 (1:100), and Twist2 (1:100) overnight at 4°C. They were then incubated with anti-rabbit, anti-goat, or anti-mouse secondary antibodies conjugated with Alexa Fluor 488, 594 or 647 (Invitrogen) for 1 h at 25°C, followed by DAPI staining. Tissue sections were mounted on glass coverslips with glycerol as the mounting medium. The corrected total nucleus fluorescence (CTNF) was calculated as the integrated fluorescence intensity (nuclear area of each cell × mean fluorescence of selected area) using ImageJ/FIJI software as previously described (Kim et al., 2019). The antibodies used in this study are listed in the key resources table.

Real-time qPCR

Total RNA was isolated from $CD140a^+CD26^+$ PFs using TRIzol (Invitrogen), and complementary DNA (cDNA) was synthesized from equal amounts of RNA using a RevertAid First Strand cDNA Synthesis Kit (Thermo). Synthesized cDNA was mixed with SYBR Green Master Mix (Bioneer), and RT–qPCR was performed on an ABI 7700HT thermal cycler (Thermo). Target gene cycle threshold (Ct) values were normalized to those of 36B4 in the same sample to determine ΔCt values and then against the control sample to calculate ΔΔCt and log fold change ($2-\Delta\Delta Ct$) values. The primers used in this study are listed in Table S6.

Western blotting

Total protein was extracted from $CD140a^+CD26^+$ PFs using RIPA lysis buffer (Millipore). The histone fraction was extracted using an EpiQuik Total Histone Extraction Kit (Epigentek) according to the manufacturer's instructions. For immunoblotting, equal amounts of the histone fractions were separated on 15% acrylamide gels and transferred to polyvinylidene fluoride membranes. The membranes were incubated with primary antibodies against H3 (1:1000) and H3K27ac (1:1000) overnight at 4°C. Then, the membranes were probed with horseradish peroxidase (HRP)-conjugated anti-rabbit IgG and anti-mouse IgG antibodies (GeneTex) for 1 h at 25°C. The resultant complexes were visualized by enhanced chemiluminescence (Thermo), captured with an Amersham Imager 680 (GE) and quantified using Amersham Imager 680 analysis software (GE).

Coimmunoprecipitation

Total protein was extracted from CD140a$^+$CD26$^+$ PFs using RIPA IP lysis buffer (Millipore). The input lysates were stored separately, and a Twist2 antibody (1 μg per immunoprecipitation, Abcam ab66031) was incubated with Protein G Dynabeads (Thermo) for 1 h at 4°C to form antibody-bead complexes. To prevent antibody coelution, we performed the antibody-bead crosslinking step using BS3 conjugation buffer (Thermo) according to the manufacturer's instructions. After preclearing, immunoprecipitation of the antibody-bead complexes was performed for 15 min at 25°C. Thereafter, the protein-antibody-bead complexes were washed three times with wash buffer (0.02% Tween 20 in PBS), and the immunocomplexes were eluted with NuPAGE LDS sample buffer (Thermo). The input lysates and dissociated immunocomplexes were analyzed by western blotting using antibodies targeting HDAC2 (1:1000), Twist2 (1:1000) and β-actin (1:1000) and secondary anti-mouse or anti-rabbit antibodies conjugated with HRP. Visualization was achieved by enhanced chemiluminescence (Thermo). The antibodies used in this study are listed in the key resources table.

Single-cell RNA-seq analysis

For scRNA-seq, dermal and epidermal single-cell suspensions were quantified with a hemocytometer and combined at a 1:1 ratio. Cells were pooled together from 2 mice per replicate. Dead cells were removed using the Dead Cell Removal Kit (MACS) according to the manufacturer's directions. Library construction was performed with the Chromium Single Cell 3′ Reagent Kit v3 Chemistry (10X Genomics) according to the manufacturer's protocol. The library was sequenced on the Illumina HiSeq X Ten platform (Illumina) at Macrogen (Korea). Transcripts were mapped to the mm10 reference genome using CellRanger v4.0.0 with the default reference package (10X Genomics). The web summary of CellRanger statistics is listed in Table S1. First, spliced and unspliced transcript reads were calculated using the velocyto v0.17 package (La Manno et al., 2018) in the CellRanger output folder. The velocyto output was merged using the loompy package and imported into the Seurat v4.0 R package (Hao et al., 2021) for quality control, dimensionality reduction, cell clustering, and differential expression analyses based on spliced expression matrices, as directed in the Seurat vignette (https://satijalab.org/seurat/). Briefly, spliced expression matrices were normalized using the sctransform function to remove confounding sources of variation, including technical variability. Then, principal component analysis (PCA) was performed, the top 20 PCs were used to run the UMAP algorithm, and the FindNeighbors and FindClusters functions were used for unsupervised clustering analysis. Dermal fibroblast clusters were identified based on Col1a1 and Pdgfra expression. For the subclustering analysis of dermal fibroblast-lineage cells, the same Seurat workflow described above was followed. Upper fibroblast lineage clusters were identified based on marker gene expression (Pdgfra, Dpp4) and the differentiation trajectory calculated based on RNA velocity (Bergen et al., 2020), and the clusters were subjected to downstream analysis to assess fate specification according to the differentiation trajectory. Upper dermal clusters were subclustered and imported into the scVelo v0.2.3 Python package for the assessment of velocity-inferred cell-to-cell transitions, pseudotime analysis, partition-based graph abstraction (PAGA) (Wolf et al., 2019), cellular ancestry showing descendants/ancestors, and velocity genes as directed in the scVelo vignette (https://scvelo.readthedocs.io/). For the subclustering analysis of timepoint samples, the same Seurat and scVelo workflow described above was followed. Differentially expressed gene analysis between cell clusters was performed using the FindMarkers function based on the nonparametric Wilcoxon rank sum test, and the results were visualized by using the EnhancedVolcano v1.12.0 package. Gene ontology analysis was performed using the gProfileR v0.7.0 package. Gene regulatory network analysis was performed to infer active TF networks using the SCENIC v1.2.4 package (Aibar et al., 2017) with the default parameters as directed on the SCENIC vignette (https://github.com/aertslab/SCENIC) using the RcisTarget database.

ATAC-seq library preparation

ATAC-seq was performed on freshly FACS-sorted CD140a$^+$CD26$^+$ cells as previously described (Buenrostro et al., 2015). Cells were pooled together from 2 mice per replicate. Briefly, cells were incubated with cold lysis buffer (10 mM Tris-HCl pH 7.4, 10 mM NaCl, 3 mM $MgCl_2$, 0.1% IGEPAL CA-630). After removing the lysis buffer, the samples were immediately subjected to a transposition reaction for 30 min at 37°C with TN5 transposase (Illumina). Transposed DNA was purified using a Qiagen MiniElute purification kit and PCR amplified over 10–15 cycles. Library construction was performed using Nextera primers (Illumina) as previously described (Buenrostro et al., 2015). ATAC-seq experiments were independently repeated two times. A total of eight samples were uniquely barcoded, and the sequencing library was prepared according to the manufacturer's guidelines (Illumina). The concentration and quality of the library were assessed by using Tape Station HSD5000 (Agilent) prior to sequencing. The libraries were sequenced on the Illumina HiSeq 2500 platform using the 50-bp paired-end setting at Macrogen (Korea).

ChIP-seq library preparation by ChIPmentation

ChIP-seq of freshly FACS-sorted CD140a$^+$CD26$^+$ cells was performed using the ChIPmentation method (Schmidl et al., 2015). Cells were pooled together from 2 mice per replicate. Briefly, the cells were fixed with 1% paraformaldehyde in PBS for 10 min at 25°C, after which glycine was added to stop the reaction. The cells were collected by centrifugation at 500 g for 10 min at 4°C and washed twice with 1 μM phenylmethyl sulfonyl fluoride (PMSF) in PBS. The pellet was disrupted with a Branson 102C sonicator with a 15% pulse for 10 s, which was repeated 7 times on ice with a MilliTUBE (Covaris) until the sizes of the fragments was within 200–700 bp. The lysate was centrifuged at 14,000 g for 5 min at 4°C, and the supernatant containing the sonicated chromatin was transferred to a new tube. The sonicated lysate was brought to a total volume of 200 μL with RIPA buffer (10 mM Tris-HCl pH 8.0, 1 mM EDTA, 140 mM NaCl, 0.1% SDS, 0.1% DOC, 1% Triton X-100, 1 μM PMSF, and 1× protease inhibitors) per immunoprecipitation. For each immunoprecipitation, Protein A Dynabeads (10 μL) were washed twice and resuspended in 0.1% BSA in PBS. The appropriate antibody was added and bound to the beads by rotation for 2 h at 4°C. An anti-H3K27ac antibody (1 μg per immunoprecipitation, Diagenode pAB-196-050) and a nonspecific IgG rabbit antibody (2.5 μg per immunoprecipitation, Millipore 12–370) were used. The tube containing the blocked antibody-conjugated beads was then placed on a magnet, the supernatant was removed, and the sonicated lysate was added to the beads for 3 h at 4°C under rotation. The beads were then washed with RIPA, RIPA-HS (10 mM Tris-HCl pH 8.0, 1 mM EDTA, 500 mM NaCl, 0.1% SDS, 0.1% DOC, 1% Triton X-100) and RIPA-LiCl (10 mM Tris-HCl pH 8.0, 1 mM EDTA, 250 mM LiCl, 0.5% NP40, 0.5% DOC) buffers. The beads were washed with cold Tris-HCl pH 8.0, resuspended in 25 μL of tagmentation reaction buffer (10 mM Tris pH 8.0, 5 mM $MgCl_2$, 10% v/v dimethylformamide) containing 1 μL of the TN5 transposase enzyme (Illumina) and incubated for 5 min at 37°C in a thermocycler. The beads were washed with RIPA and cold Tris-HCl pH 8.0 and then incubated with 70 μL of elution buffer (10 mM Tris-HCl pH 8.0, 5 mM EDTA, 300 mM NaCl, and 0.4% SDS) containing 2 μL of Proteinase K (NEB) for 1 h at 55°C and for 6 h at 65°C; the supernatant was transferred to a new tube. Transposed DNA was purified with a Qiagen MiniElute purification kit and PCR amplified using Kapa HiFi HotStart ReadyMix (Kapa Biosystems). The enriched libraries were purified using SPRI AMPure XP beads at a bead-to-sample ratio of 1:1, followed by size selection using AMPure XP beads to recover libraries with a fragment length of 200–400 bp. Library construction was performed using the TruSeq ChIP Library Preparation Kit (Illumina). The libraries were sequenced on the Illumina HiSeq 2500 platform using the 100-bp paired-end setting at Macrogen (Korea).

ATAC-seq and ChIP-seq analysis

Sequencing reads were aligned to the mm10 mouse genome (UCSC) using Bowtie2 v1.1.1 (Langmead and Salzberg, 2012) with the parameter ''-X2000 –very-sensitive'' for paired-end reads. Duplicates were removed using Picard v2.7.1. The quality of ATAC-seq data was assessed with ATACseqQC v1.18.0 (Ou et al., 2018) to check the library complexity, fragment size distribution, promoter/transcript body score, nucleosome-free region score and transcription start site (TSS) enrichment score. Peaks for each replicate were called using MACS2 v2.1.2 (Zhang et al., 2008) in BAMPE mode. Differential signal analysis was performed using DESeq2 v1.32.0 (Love et al., 2014). Briefly, count matrices were generated by measuring the signal from each replicate in an experiment with a nonredundant union peak set representing peak calls across all three timepoints. PCA was performed using signals within peaks. Plotting of the ATAC signal of TSSs was performed using soGGi v1.24.1 (Dharmalingam et al., 2021) to generate plots of the average signal across TSSs for different fragment length ranges to show nucleosome-free, mono-nucleosome and di-nucleosome signal profiles. The overlap of ATAC peaks among samples was calculated using the overlap matrix generated by soGGi with the vennDiagram function. ChIPseeker v1.28.3 (Yu et al., 2015) was used to annotate the genomic features of peak regions with the TxDb.Mmusculus.UCSC.mm10.knownGene package. The peak files for each PD0, PD2 and PD4 sample were merged to obtain a consensus peak file representing a total of 57,954 peak regions that were called at least one time at all three timepoints. The DeepTools v3.4.2 (Ramírez et al., 2016) bamCoverage (for ATAC samples) or bamCompare (for ChIP samples vs. IgG samples) function was used to generate bigWigs of BAM files for the consensus peak regions. For the semiquantitative analysis of ChIP-seq data, the H3K27ac signal of each sample was normalized to the merged input signal by using the scale factors calculated based on the total H3K27ac protein-to-H3 protein ratio as previously proposed (Orlando et al., 2014). The deepTools computeMatrix function was used to evaluate the ATAC and H3K27ac signals of ±5 kbp regions around TSSs plotted for each sample. Profileplyr v1.7.0 (Carroll and Barrows, 2021) was used to perform k-means clustering of ATAC peaks and generate box plots and heatmaps according to cluster domains. Cluster domains identified from the ATAC peaks of the PD0, PD2 and PD4 samples were consistently applied to TSA-PD4 samples as well as the H3K27ac signal to generate box plots and heatmaps. Ontology analysis was performed using the Genomic Regions Enrichment of Annotation Tool (GREAT) with the whole mouse genome (GRCm38/mm10) as the background. The ATAC and H3K27ac signal tracks were presented by using Integrative Genomics Viewer (IGV) software (Broad Institute). The peak regions and corresponding ATAC and H3K27ac signals from this study are listed in Tables S4 and S5.

Motif analysis

The unique chromatin regions were calculated using BEDtools v2.25 with the parameter ''subtract -a'' by subtracting PD2 or PD4 peak regions from PD0, PD2, or TSA-PD4 peak regions. To identify enriched sequence motifs that matched TF binding sites, we performed *de novo* sequence motif discovery using HOMER (Heinz et al., 2010) applied to the ±200 bp sequences around ATAC peak summits with the default settings. Motifs were reported according to p values that were considered significant and expression in dermal fibroblasts.

TF footprinting analysis

To compare the Twist2 activity changes based on differential binding in open chromatin regions of PD0, PD2, PD4 and TSA-PD4 samples, we performed TF footprinting analysis using the HINT algorithm (Gusmao et al., 2016) for ATAC-seq data (Li et al., 2019), which is a framework for identifying active TF binding sites in open chromatin data. We used BAM files and corresponding peak files from ATAC replicates as input, which were preprocessed based on read alignment with Bowtie2 and peak calling with MACS2. Differential footprinting analysis was performed to generate average signal profiles around Twist2 binding sites from each replicate within an experiment, and the two ATAC-seq experiments showed similar results regarding the binding activity of Twist2. The cut-site probability at each position in the ±100 bp regions around Twist2 binding sites was used to calculate statistically significant differences between samples.

QUANTIFICATION AND STATISTICAL ANALYSIS

Statistics and reproducibility

No statistical methods were used to predetermine the sample size. The experiments were not randomized, and the investigators were not blinded to the allocation during the experiments and outcome assessment. The numbers of biological replicates are specified in the figures and figure legends. Data are presented as the mean ± s.e.m., and the biological replicates are shown in the graph backgrounds. Two-tailed unpaired Student's t test or Welch's two-sample t test was used to analyze datasets with two or more than three groups. The generation of data plots and statistical analyses were performed using Excel (Microsoft), Prism (GraphPad) and R (R Foundation). p values <0.05 indicated significance and are presented as follows: *$p < 0.05$, **$p < 0.01$, ***$p < 0.001$, ****$p < 0.0001$; the exact p values are supplied in the figures and figure legends.